X-ray Coherent Scatter Imaging for Intra-operative Margin Detection in Breast Conserving Surgeries

by

Manu N. Lakshmanan

Department of Biomedical Engineering
Duke University

Date: _____

Approved:

_____
Anuj J. Kapadia, Supervisor

_____
Sina Farsiu (Co-chair)

_____
Joseph Y. Lo (Co-chair)

_____
Shelley Hwang

_____
Gregg Trahey

_____
Ehsan Samei

Dissertation submitted in partial fulfillment of the requirements for the degree of
Doctor of Philosophy in the Department of Biomedical Engineering
in the Graduate School of Duke University
2015

Abstract

X-ray Coherent Scatter Imaging for Intra-operative Margin Detection in Breast Conserving Surgeries

by

Manu N. Lakshmanan

Department of Biomedical Engineering
Duke University

Date: _____

Approved:

_____
Anuj J. Kapadia, Supervisor

_____
Sina Farsiu (Co-chair)

_____
Joseph Y. Lo (Co-chair)

_____
Shelley Hwang

_____
Gregg Trahey

_____
Ehsan Samei

An abstract of a dissertation submitted in partial fulfillment of the requirements for the degree of Doctor of Philosophy in the Department of Biomedical Engineering in the Graduate School of Duke University
2015

Abstract

One of the challenges facing clinical practice today is intra-operative margin detection in breast conserving surgeries (BCS) or lumpectomy procedures. When a surgeon removes a breast tumor from a patient during a BCS procedure, the surgically excised tissue specimen is examined to see whether it contains a margin of healthy tissue around the tumor. A healthy margin of tissue around the tumor would indicate that the tumor in its entirety has been removed. On the other hand, if cancerous tissue is at the surface of the specimen, that would indicate that the tumor may have been transected during the procedure, leaving some residual cancerous tissue inside the patient. The most effective intra-operative real-time margin detection techniques currently used in clinical practice are frozen section analysis (FSA) and touch-prep cytology. These methods have been shown to possess inconsistent accuracy, which result in 20% to 30% of BCS patients being called back for a repeat BCS procedure to remove the residual tumor tissue. In addition these techniques have been shown to be time-consuming–requiring the operating room team to have to wait at least 20 minutes for the results. Therefore, there is a need for accurate and faster technology for intra-operative margin detection.

In this dissertation, we describe an x-ray coherent scatter imaging technique for intra-operative margin detection with greater accuracy and speed than currently available techniques. The method is based on cross-sectional imaging of the differential coherent scatter cross section in the sample. We first develop and validate

a Monte Carlo simulation of coherent scattering. Then we use that simulation to design and test coherent scatter computed tomography (CSCT) and coded aperture coherent scatter spectral imaging (CACSSI) for cancerous voxel detection and for intra-operative margin detection using (virtual) clinical trials. Finally, we experimentally implement a CACSSI system and determine its accuracy in cancer detection using tissue histology.

We find that CSCT and CACSSI are able to accurately detect cancerous voxels inside of breast tissue specimens and accurately perform intra-operative margin detection. Specifically, for the task of individual cancerous voxel detection, we show that CSCT and CACSSI have AUC values of 0.97 and 0.94, respectively. Whereas for the task of intra-operative margin detection, the results of our virtual clinical trials show that CSCT and CACSSI have AUC values of 0.975 and 0.741, respectively. The gap in spatial resolution between CSCT and CACSSI affects the results of intra-operative margin detection much more than it does the task of individual cancerous voxel detection. Finally, we also show that CSCT would require on the order of 30 minutes to create a 3D image of a breast cancer specimen, whereas CACSSI would require on the order of 3 minutes.

These results of this work show that coherent scatter imaging has the potential to provide more accurate intra-operative margin detection than currently used clinical techniques. In addition, the speed (and therefore low scan duration: 3 min) of CACSSI, along with its ability to automatically classify cancerous tissue for margin detection means that coherent scatter imaging would be much more cost-effective than the clinical techniques that require up to 20 minutes and a trained pathologist. With the cancerous voxel detection accuracy of a 0.94 AUC and scan time of on the order of 3 minutes demonstrated for coherent scatter imaging in this work, coherent scatter imaging has the potential to reduce healthcare costs for BCS procedures and rates of repeat BCS surgeries. The accuracy for CACSSI can be considerably

improved to match CSCT accuracy by improving its spatial resolution through a number of techniques: incorporating into the CACSSI reconstruction algorithm the ability to differentiate noise from high frequency signal so that we can image with higher frequency coded aperture masks; implementing a 2D coded aperture mask with a 2D detector; or acquiring additional angles of projection data.

To my mom, Sushila, for always believing in me.

And to my dad, Ramaswamy, for being my best friend all these years.

Some people see things as they are and say why?

I dream things that never were and say, why not?

—Robert F. Kennedy, 1968

Contents

List of Tables

List of Figures

List of Abbreviations and Symbols

Symbols

$d\sigma_{coh}/d\Omega$	Differential coherent scatter cross section.
$\mathcal{R}^{-1}\{\}$	Inverse radon transform, i.e., filtered back-projection.
N_s	Number of scattered x-rays measured.
A_{max}	Maximum case accuracy in ROC statistics, from optimal variable decision criterion value.
N_t	Number of transmitted x-rays measured.
θ	X-ray scatter angle.
E	Energy of measured x-ray.
FF	Form factor.
Φ	Probability density function for coherent scattering.
h	Planck's constant.
l^2	L-2 or Euclidean norm.
c	Speed of light in vacuum.
n_0	Electron density inside the sample.
$\triangle\Omega$	Solid angle subtended by a detector pixel from the sample.
q	Momentum transfer of measured x-ray.
u	Coded aperture mask spatial frequency.
w	X-ray pencil beam diameter.
x	Coordinate perpendicular to x-ray beam, along the height.

y	Coordinate perpendicular to x-ray beam, along the direction of the linear detector array.
z	Coordinate along direction of x-ray beam.
z_d	Location of detector.
z_m	Location of coded aperture mask.
z_o	Location of the object.

Abbreviations

AUC	Area under the curve.
BCS	Breast conserving surgery.
CT	Computed tomography.
CSCT	Coherent scatter computed tomography.
CACSSI	Coded aperture coherent scatter spectral imaging.
ECM	Extracellular matrix.
ESF	Edge-spread function.
FOV	Field-of-view.
FSA	Frozen section analysis.
H&E	Hematoxylin and eosin histology staining.
IAA	Independent atom approximation.
MAP	Maximum a posteriori.
MLE	Maximum likelihood estimation.
MTF	Modulation transfer function.
MC	Monte Carlo.
A	Accuracy of cases in ROC analysis.
TN	True negative cases in ROC analysis.
N	Total number of cases in ROC analysis.
TP	True positive cases in ROC analysis.

ROC	Receiver-operator characteristics.
FN	False negative cases in ROC analysis.
FP	False positive cases in ROC analysis.
TV	Total variation regularization method.
XRD	X-ray diffraction.
XCAT	eXtended CArdia-Torso phantom.

Acknowledgements

There are so many people who made it possible for me to carry out the research presented in this dissertation.

I first must thank my advisor, Prof. Anuj Kapadia. I believe that the quality of the work presented in this dissertation as well as in my other publications and presentations are due to his mentorship. During my initial and formative years in graduate school, the hours he would spend meeting with me individually from week-to-week helped me develop as a researcher. And seeing his light on in his office late into the evenings inspired me. Throughout my graduate career, he's made sure that I developed, grew, and received recognition by giving me numerous opportunities to present and publish my research. I could not have asked for a better person to work with all these years.

The next two most important people without whom this work would not have been possible are Brian Harrawood and Prof. Joel Greenberg. Brian developed a countless number of the software tools and the foundation upon which the Monte Carlo simulations in this dissertation were built upon. Without him, the simulation studies I carried out in this dissertation would have taken a few decades to complete. Joel provided the support for my implementation of the CACSSI and experimental parts of this work. Furthermore, he spent several months working with me in the lab, teaching me how to set up and conduct x-ray experiments. Throughout the years Brian and Joel have helped me troubleshoot scores of problems that arose in

my research. In addition to the research support they provided, it was a pleasure getting to spend so much time working with both of them.

Robert Morris and Katie Albanese started working in our research group at the start of this year, but their contributions to the experimental part of this work proved to be crucial to my dissertation. Robert painstakingly acquired the CACSSI dataset that we ultimately used to validate with the tissue histology and he helped coordinate our collaboration with the Pathology department. In addition, Katie and Robert kept our weekly lab meetings light-hearted always.

There are so many other people at Duke who helped with various aspects of my research along the way. Prof. Ehsan Samei provided us with his x-ray lab to carry out our experiments and he provided critical inputs on the vision and direction of my project. Dr. Shelley Hwang provided us with the clinical guidance and the idea for the clinical application for this project. For designing the virtual breast tissue specimens, Prof. Paul Segars provided us with the breast XCAT phantoms, and Justin Solomon and Dr. Nooshin Kiarashi provided the breast tumor geometries. Prof. Sina Farsiu provided us with the idea of using ROC analysis for cancerous voxel classification. Prof. Kingshuk Roy Choudhury helped us with the statistical analysis to determine the sample size we needed for the virtual clinical trials. Prof. Scott Wolter carried out the x-ray diffraction measurements that we used to model the non-biological materials in the simulations. Prof. David Brady's coherent scatter imaging project for the Department of Homeland Security provided the foundation from which my dissertation project was born. Dr. Shannon McCall analyzed the tissue histology results. Prof. Joseph Lo and Dr. Xiaobo Lai shared with us their model for spiculations in breast tumors. Prof. Martin Tornai and Dr. Jainil Shah acquired x-ray CT scans of our breast tissue specimens. Dr. Matt Belley developed the initial strategy for modifying the Monte Carlo physics code to incorporate diffraction and Dr. Pooyan Sahbaee did the initial testing of the code.

I'd like to thank my committee members, Profs. Sina Farsiu, Joseph Lo, Ehsan Samei, Shelley Hwang, and Gregg Trahey for providing me with guidance that was helpful for my progress in my final year, for their support and encouragement, and for making my prelim exam (relatively) painless. Brian Harrawood and Dr. Juan Carlos Ramirez-Giraldo helped me practice for my prelim and provided critical feedback to help me improve.

I'd like to thank my friends who kept me in good spirits during this journey. Although I cannot personally name all of them here, I'd like to recognize some who played especially important roles during my time at Duke. Drs. Pooyan Sahbaee, Nooshin Kiarashi and Sukantadev Bag, thank you for the four trips per day to the kitchen to get coffee, the basketball games on my cubicle hoop, and your company in the RAILabs late into the evenings. Grant Fong, Dr. Patrick Pan, and Ming Hsiao, thank you for all the workouts at Wilson. Rohan Patil, Anurodh Tripathi, Yeongun Ko and Janell Harhi, thank you for the Sunday morning and Tuesday evening top-rope climbing sessions at the Triangle Rock Club. Brad Rubin, thank you for the Saturday morning pickup basketball games at Brodie. Yaying Feng, Doug Smith, Elisa Peterson, Kevin Campbell, and Jordan Churchill, thank you for the "Murphy's Committee meetings" at James Joyce and the formal-attire dinners at Mami Nora's that preceded them. Sonia George, Sparsh Agrawat, Seetha, and Rohan Virgincar, thank you for your enduring friendship from the year I arrived in Durham. James Davis, thank you for inspiring me to "still believe."

I would like to acknowledge the support of the many funding sources and organizations that made it possible for me to conduct and present my research: the Ravin Advanced Imaging Labs, the Department of Biomedical Engineering first-year Ph.D. student fellowship and conference travel award; the IEEE Nuclear Science Symposium and Medical Imaging conference trainee grant; the Duke Graduate School conference travel award; the Department of Defense Breast Cancer Research Program

(through Award W81XWH-09-1-0066); the Center for Molecular and Biomolecular Imaging at Duke University; and the Department of Homeland Security, Science & Technology Directorate, Explosives Division (through contract HSHQDC-11-C-0083).

Finally, this dissertation is dedicated to my parents–Ramaswamy and Sushila. Mom, thank you for persistently reminding me every single day to always keep faith. And move over Dad; there's a new Dr. Lakshmanan in town.

Manu Lakshmanan
Durham, North Carolina
December 2015

1

Introduction

Parts of the text in this chapter have been published in Physics in Medicine and Biology, 60(16): 63355, 2015 [11] and Nuclear Instruments and Methods in Physics Research, Section B, 335: 31-38, 2014 [12].

In the United States, about one in eight women will develop invasive breast cancer and about one in thirty-six will die of it [13], making its treatment an utmost concern and making it one of the most commonly treated and researched diseases. Because such a large number of patients are treated for breast cancer, innovations in breast cancer treatment have tremendous potential for impact. The diagnosis and imaging of breast cancer is one of the most challenging clinical tasks because of (1) the limited contrast between cancerous tissue and dense healthy breast tissue; and (2) the irregular spiculated shapes of breast tumors that make it difficult to identify the total extent of disease. As a result, there is a pressing need for innovations in breast cancer diagnosis and treatment to improve efficiency at all stages of breast cancer treatment: screening, diagnosis, surgery, and therapy. In this dissertation, we focus on developing a breast cancer imaging technology to improve the efficiency of surgical treatment of breast cancer.

1.1 Clinical problem

In this section, we review the current clinical standard of care for breast cancer surgical therapy, its limitations, and alternative proposed technologies to overcome these limitations.

1.1.1 Current clinical practice

Once a breast tumor is detected in a patient, treatment can include a multitude of options, e.g., chemotherapy, radiation treatment, surgery, or any combination of these. In cases of surgical interventions, surgery may be of one of two types: (a) breast-conserving surgery (BCS)–in which only the tumor along with some surrounding healthy tissue is removed; or (b) mastectomy–in which the entire cancerous breast is removed. In most cases, unless the cancer is late stage, both treatment options are available to the patient. Patients often choose BCS (59% of the time [14]) over mastectomy (chosen in 36% of cases) because of its better cosmetic results and because it provides survival rates as high as mastectomy [13, 15].

During a BCS procedure, the surgeon removes a piece of tissue containing the tumor and a minimal amount of surrounding healthy tissue as a safety margin. This safety margin is to ensure that no cancer cells were left behind in the breast. In a BCS procedure, once the surgeon has removed the affected region of breast tissue, the removed tissue specimen must be analyzed–either by the surgeon visually or through some other technique such as frozen section analysis (discussed below) or touch-prep cytology–in order to confirm that all cancerous tissue has been successfully removed from the patient, i.e., the surgeon must ensure that the margin of the tumor contains no cancerous cells at the edge of the specimen (a negative margin). The presence of cancerous cells at the edges of the specimen (a positive margin) indicates that more cancerous tissue may still remain in the patient and that the patient must

undergo a re-excision of tissue in order to ensure that the entire tumor has been removed. This process involves performing a repeat follow-up surgery that poses risk and complications for the patient. In contrast, if the specimen has negative margins (i.e., no cancerous cells are present at the edges), no re-excision is necessary and the BCS procedure can be deemed complete.

The gold standard for evaluating margins is histology analysis of the tissue by a pathologist. This analysis typically entails a hematoxylin and eosin (H&E) stain performed on paraffin-embedded tissue sectioned serially [16]. The H&E staining is performed post-operatively to determine whether the surgically resected tissue contains negative or positive margins. The processed tissue slides are analyzed by a pathologist, who seeks to confirm the presence of the tumor in the resected tissue section surrounded by a non-cancerous margin. "Negative margins (sometimes alternatively called "clear margins") imply that the entire tumor was removed from the patient, whereas "positive margins" imply that the tumor may not have been removed in entirety. While the H&E staining method is effective, the processing time for the technique ranges from several days to over a week [17]. Hence, it cannot be performed intra-operatively and must be performed in the days following surgery. If the pathologist reports positive margins, the surgeon must recall the patient for another BCS procedure to ensure complete removal of tumor tissue.

Repeat surgeries are a pressing clinical problem because they occur often and carry serious consequences for the patient and for the payer. Studies have reported that between 20% to 30% of BCS patients require repeat surgeries [18]. Performing multiple BCS procedures is not only costly in terms of resources to healthcare providers, but is taxing on the patient: repeat procedures can cause for the patient additional discomfort, additional surgical complications, worsened cosmetic outcomes for the breast, and they have been associated with driving patients to pursue bilateral mastectomy [19]. They can also cause additional emotional stress for the families of

the patients [19,20]. If an accurate margin assessment process could be performed in real time, i.e., during the original BCS procedure, then the surgeon could better ensure removal of all tumor tissue in a single surgery, potentially reducing the number of repeat surgeries and associated consequences.

1.1.2 Limitations of existing clinical intra-operative margin detection techniques

For intra-operative evaluation of margins, two clinical methods are currently practiced:

1. frozen-section analysis (FSA) [16], in which the specimen is frozen and thin sections are cut for pathological assessment, and

2. touch-prep cytology [21], in which glass slides are touched to the specimen and are then stained for pathological analysis.

Given their associated costs, both techniques have had limited effectiveness, with more than 95% of hospitals (including Duke, and MD Anderson Cancer Center) opting not to use them routinely. Most hospitals instead have the surgeon visually inspect the resected specimen, a technique found to be inaccurate in at least 25% of cases [22]. The specificity and sensitivity with which FSA and touch-prep cytology gauge margins as reported in the literature are: 65 to 91% sensitivity and 86 to 100% specificity for FSA, and 38 to 100% sensitivity and 85 to 100% specificity for touch-prep cytology [21]. This large variability in the accuracies obtained with touch-prep cytology likely exists because it is unable to identify close margins [23]. The large variability in the accuracies obtained with FSA likely exists because it performs poorly with fatty breast tissue, suffers from freezing artifacts in adipose tissues, and it samples only a small portion of the surgical margin [24,25]. The small percentage of hospitals even attempting intra-operative margin evaluation, along with the wide

ranging accuracies reported for the techniques, explains the large percentage (20 to 30%) of BCS patients requiring repeat surgery [18].

Furthermore, the time and resources that these techniques require are significant, with a turn-around time that includes 17-20 minutes for the procedure plus wait time for an available pathologist [13,26]. There is a pressing need for a more accurate and faster margin detection technique during BCS procedures.

1.1.3 Alternative proposed margin detection techniques

In order to be effective for margin detection, an imaging technique should be able to clearly delineate healthy and malignant tissue with sub-millimeter spatial resolution in order to visualize margins. The challenge for an imaging technique in identifying tissue as either healthy or malignant lies in the considerable degree of heterogeneity present in healthy breast tissue as well as the irregular shapes of tumors (e.g., spiculated tumor shape in Fig. 1.37 in Ref. [27]).

Several new diagnostic techniques are being developed for margin detection, including the application of radio waves to measure electromagnetic properties [28] and several optical imaging methods [24, 29–31]. However, radio waves have not been used for image reconstruction, and optical photons lack penetrating power. As a result, these techniques are not able to reconstruct full three-dimensional images of the tissue sample, but instead are only able to provide information to a depth of a few millimeters into the specimen. Although the penetration depth of optical imaging methods would be sufficient to detect the negative margins in most scenarios, the lack of penetration depth precludes the ability to confirm the presence of the tumor within the resected section (a particular concern in the case of multi-focal disease). An ability to visualize a three-dimensional representation of the entire tumor inside the resected tissue would provide the surgeons strong confirmation on the outcome of the surgery, even in cases of multi-focal disease.

Another x-ray imaging technique that has been shown to potentially aid conventional x-ray imaging in cancer is x-ray phase contrast imaging (XPCI): the phase shift cross section in XPCI is nearly one thousand times larger than the x-ray absorption cross section for light elements such as those in biological tissue [32]. XPCI therefore has the potential to observe structure inside soft tissue with greater contrast than is possible by measuring transmitted x-rays. Specialized implementations of XPCI such as grating based phase contrast imaging [33] makes it possible to perform XPCI using conventional x-ray tubes, and analyzer-based scatter imaging [34], which employs phase contrast with ultra-small-angle x-ray scattering, also improves contrast in soft tissue. However XPCI only provides contrast at boundaries and is unable to provide material-specific signatures over large volumes and a broad range of material types [35].

Current methods of margin assessment therefore suffer from the following limitations:

1. wide-ranging sensitivity and specificity values;
2. limited depth of tissue penetration;
3. 20%-30% call-back rates; and
4. moderately long wait times (17-20 minutes).

In order to address the limitations of these margin detection techniques, we propose to develop and demonstrate in this dissertation a coherent scatter imaging system for cancerous tissue identification that provides three-dimensional images of the distribution of cancerous tissue inside of surgically removed tissue for margin detection.

1.2 Coherent scatter imaging

The technology that we develop in this dissertation uses the signal from x-ray coherent scattering in order to reconstruct cross-sectional images of the sample. Therefore, in this section we review the physics of coherent scattering, its various medical and non-medical applications, its applicability for breast cancer detection, its specific applicability for intra-operative margin detection, and the potential impact it could have on breast cancer treatment.

1.2.1 Physics of coherent scattering

The utility of scattered x-rays was discovered when Friedrich et al. [36] and Bragg & Bragg [37] were able to show that because the interatomic spacing of solids coincides with the wavelength range of x-rays (on the order of angstroms), the interference of x-rays reflected off the atoms in a given solid produces an intensity pattern that can be used to investigate the structure of the solid. This interference of reflected electromagnetic waves by a solid is commonly referred to as Bragg diffraction. Shortly after 1914, Bragg diffraction led to the birth of x-ray crystallography for determining the atomic and molecular structures of small homogenous samples, e.g., work by Watson et al. [38] in determining the double-helix structure of DNA that revolutionized molecular biology.

However, x-ray crystallography cannot be directly applied for medical applications because it requires the sample to be crystallized, i.e., in the form of a well-ordered crystal and free from any contaminants. Debye & Scherrer [39], and Hull [40] showed that diffraction could be used to probe information about non-crystallized samples as well, introducing the concept of powder diffraction. If a sample, even a non-ordered-crystal, is instead present in a random powdered or amorphous form such as human tissue, then due to the random orientation of the microcrystalline

structures in the sample with respect to each other, the orientational averaging leads to symmetry in the azimuthal angle of the diffracted x-rays. In contrast, the probability distribution of scattering in the polar angle is unique to the sample and depends on its structural properties. Due to this circular symmetry in the azimuthal angle, the diffracted x-rays come off the sample as concentric cones of radiation that appear as a ring pattern when measured on a piece of film or on a flat detector. The radii and intensity of the rings are unique to the scattering sample. Thus, powder diffraction patterns have been studied extensively for use as a potential diagnostic tool in medical imaging, the results of which will be discussed in the next subsection.

1.2.2 Applications of coherent scatter measurements

These power diffraction patterns have been investigated for material identification for medical [41–43] and homeland security [44, 45] applications. These studies have shown that scattered x-rays can provide higher signal-to-noise ratios (SNR) in identifying certain tissue types (medical) and sensitive materials (homeland security) than is currently possible using transmitted x-rays.

In homeland security applications, Madden et al. [45] and Harding [46] proposed systems for explosives detection in suitcases that first acquired a transmission image of the suitcase, followed by an x-ray diffraction image of objects that raised suspicion in the transmission image. They argued that x-ray diffraction provided orthogonal information to transmission measurements and therefore x-ray diffraction could be used as a second automatic screening in order to reduce the number of bags that needed to be manually opened and inspected. There are also several clinical applications where coherent scatter imaging could prove beneficial because of its ability to image molecular structure. In medical applications, several studies [2, 4, 47, 48] have shown that there exist significant differences in the scatter signatures from cancerous and healthy tissue, for example in the blood [42] and bone [49]. However, the appli-

cation where the contrast in coherent signal is strongest is for differentiating healthy and cancerous breast tissue, which is the subject of a far greater number of coherent scatter studies.

1.2.3 Coherent scatter signal from breast cancer

Several studies [1, 2, 47, 50, 51] have measured the coherent scatter signals from adipose, fibroglandular, normal (i.e., 50/50 adipose/fibroglandular mix) and carcinoma breast tissues. All of these studies have found that the differential coherent scatter cross section ($d\sigma_{coh}(q)/d\Omega$) curves differ considerably between the four tissue-types (see Fig.1.1) due to variations at the molecular level (discussed below). The differences in $d\sigma_{coh}(q)/d\Omega$ are large enough to allow differentiation of adipose, fibroglandular, normal and cancerous tissue samples based on the angular distribution of coherent scattering measured from them [2–8].

Lewis et al. [52] and Theodorakou & Farquharson [53] speculate that healthy and cancerous tissue exhibit different coherent scatter properties because of the extracellular matrix (ECM) in the tissue. The ECM has been shown to give characteristic coherent scatter patterns due to its well-ordered structure. Specifically, when collagen molecules pack into bundles called fibrils, its structure has a periodic pattern with period (sometimes referred to as the d-spacing) of 65 nm [53, 54]. The disruption of the structure of the ECM has a known association with cancer. In the case of breast cancer, tumor invasion has been shown to be associated with increased synthesis of fibrils and a much less regular organization of these fibrils [53, 55].

Although many studies have used coherent scatter measurements to differentiate healthy and cancerous breast tissue samples, the problem of intra-operative margin detection and most other clinical breast imaging problems require the ability to image the distribution of healthy and malignant tissue within the specimen in 3D. In such cases, the ability to spatially resolve the origin of the scatter signal to a

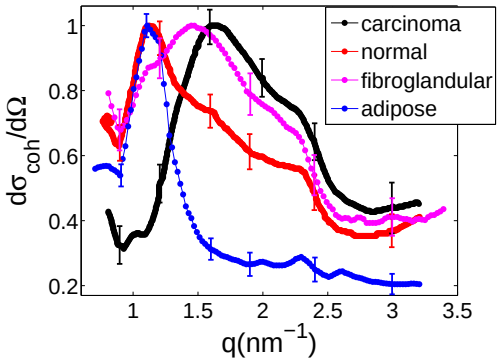

FIGURE 1.1: Using data taken from [1], we show the differential coherent scatter curves (scaled to have a maximum value of unity) as a function of q (i.e., momentum transfer, which is introduced in Chapter 2) for the four types of breast tissue modeled in this work. (Normal tissue is defined as a 50/50 adipose/fibroglandular mix). The scatter curves for all four types of tissue are significantly and reproducibly different from each other and have been successfully used in prior studies [2–8] to consistently classify cancerous and healthy tissue samples.

point within the sample would allow one to reconstruct an image of the sample that can be used for spatially-resolved tissue discrimination. Studies have shown that scatter imaging can be used to spatially resolve different materials using computed tomography techniques [56, 57] or coded apertures [58].

1.2.4 Suitability of x-ray coherent scatter imaging for margin detection

The application of coherent scatter imaging to the clinical problem of intra-operative margin detection is suitable for the following three reasons.

1. The relatively small size of resected breast specimens provides the ability to generate a low-noise image using coherent scatter. A source of noise in coherent scatter imaging that must be considered is multiple scattering. Based on the approximations made in the theoretical development of coherent scatter image reconstruction, multiple scattering can be neglected if the object size is limited to less than three half-value layers [59], which for the case of diagnostic x-rays and human tissue is ∼10 cm. Resected breast specimens in BCS procedures

are less than 10 cm in size, making noise from multiple scattering in coherent scatter imaging negligible.

2. The 0.5 mm resolution of coherent scatter imaging (see Section 1.3.1 below) makes it well-suited for the task of margin detection since desirable tumor margins are on the order of ∼2 mm.

3. The margin detection techniques currently being used in hospitals have a wide range of variability in their levels of accuracy, as discussed previously in Section 1.1.2.

1.2.5 Potential impact of coherent scattering imaging for intra-operative margin detection

This project proposes to develop a coherent scatter imaging technique to improve intra-operative margin detection during breast conserving surgery (BCS). Such technology could result in reduced rates of re-operations in BCS patients, thereby saving valuable time and resources for patients and the healthcare system.

The use of a compact coherent scatter imaging device that would perform accurate margin detection would substantially reduce the costs involved in treating breast cancers and improve patient experience. An imaging device for margin detection–even if it only gave the same level of accuracy as current margin detection techniques (e.g., FSA)–would provide results to the surgeon more quickly and at a lower cost than FSA and touch-prep cytology because using an imaging device would not require tissue processing nor the manual analysis of an on-site trained pathologist, both of which come with considerable time and monetary costs.

In addition to reducing time and monetary costs, coherent scatter imaging has the potential to provide improved accuracy beyond the wide-ranging accuracies of FSA and touch-prep cytology that was discussed previously in Section 1.1.2. Because coherent scatter imaging has the potential to generate sub-millimeter cross-sectional

images of the resected specimen, it can be used to sample the entire surgical margin, resulting in improved margin detection accuracy and reduced need for repeat surgeries.

Alternatively, this device could be used to supplement and confirm staining margin detection techniques (e.g., FSA and touch-prep cytology), in which case the device would improve margin detection accuracies while not reducing the overall wait time for margin detection results during the surgery. This improved accuracy would reduce the rate for repeat surgeries and therefore it would still reduce the average cost of breast cancer treatment per patient that a hospital incurs.

In the next section, we review the different coherent scatter imaging techniques available for development for intra-operative margin detection.

1.3 Coherent scatter imaging techniques

The coherent scatter signal from healthy and cancerous breast tissue samples are significantly and reproducibly different from each other as pointed out in the previous section. Therefore, we propose to develop coherent scatter imaging systems that can delineate (through a 2D or 3D image) the presence of healthy and cancerous tissue inside small samples such as those removed in BCS procedures. In this section, we review the two major categories of techniques available for using coherent scattering for cross-sectional imaging: (a) those that use computed tomography techniques, and (b) those that use coded apertures. In the first category of computed tomography, we choose to pursue coherent scatter computed tomography (CSCT). CSCT is the most fundamental volumetric coherent scatter imaging technique (e.g., analogous to first generation x-ray CT) and therefore its effectiveness for breast cancer imaging must be studied and assessed before attempting to implement more complex coherent scatter imaging designs (e.g., coded aperture techniques, fan beam geometries, etc.). We pursue the second category of using coded apertures because they would provide

a speedup over CSCT by an order of magnitude by eliminating the need to rotate the sample, and would therefore make coherent scatter imaging a fast imaging technique in the operating room.

1.3.1 Coherent scatter computed tomography (CSCT)

CSCT was the first coherent scatter imaging technique implemented in 1985 by Harding et al. [60] when they showed that it can provide contrast between materials that otherwise would not show contrast in conventional CT imaging. In recent years, CSCT has been shown to provide contrast between healthy and cancerous breast tissues in simple-geometry breast cancer models [61] and very low-resolution images have been generated of real breast cancer specimens [6].

Giffiths et al. [62] studied the spatial resolution of a CSCT system and were able to achieve 500-μm resolution. They also concluded that the spatial resolution can certainly be improved below 500 μm through the use of finer collimation. The spatial resolution of CSCT, its demonstrated ability for material identification [63–65] and its development for medical imaging in a number of prior studies [66] make it a natural choice for initial coherent scatter imaging development for a new clinical application such as intra-operative margin detection.

However, what may be the most concerning limitation of CSCT as a clinically feasible imaging technique is scan time. In order to maximize the ratio of coherent scatter signal to x-ray flux incident upon the sample, CSCT data acquisition must be performed using a first-generation raster scan using a pencil beam. Raster scanning a pencil beam across a sample and then repeating for a series of projection angles and tomographic slices in order to reconstruct a three-dimensional image of the sample may not be possible within the time constraints for a given clinical application. On the other hand, coded aperture coherent scatter imaging techniques provide the capability of single-angle cross-sectional imaging, thereby reducing the overall scan

time.

1.3.2 Coded aperture coherent scatter spectral imaging (CACSSI)

Other research groups have investigated a number of ways for reducing the scan time: fan-beam CSCT [63, 64, 67], selected volume tomography (SVT) [68], kinetic depth effect x-ray diffraction (KDEXRD) [69], coded aperture x-ray scatter imaging (CAXSI) [70], structured illumination coherent scatter imaging (SICSI) [35], and coded aperture coherent scatter spectral imaging (CACSSI) [71]. Of these techniques, those that employ a coded aperture (i.e., CAXSI, SICSI and CACSSI) are the only techniques for which real-time volumetric imaging through a single snapshot is possible, whereas the other techniques (i.e., fan-beam CSCT, SVT, and KDEXRD) require the acquisition of multiple measurements. When a coded aperture is placed in between the sample and the detector, it spatially modulates the scattered X-rays by a frequency dependent on the location of the scatter origin. By identifying the origin of scatter along the pencil beam, the coded aperture enables reconstruction of images of the sample without any need for tomographic rotation. Therefore, investigating and comparing a coded aperture technique with respect to CSCT for reduced scan time can guide the development of a clinical coherent scatter system with high levels of accuracy and short scan times.

Among the three coded aperture techniques, CACSSI may be the best suited for clinical development. CACSSI has been shown to give superior spectral resolution (i.e., material discrimination ability) compared to CAXSI [71], which is a critical system strength for the task of differentiating cancerous and healthy breast tissue with a high level of accuracy. In addition, the SICSI technique requires the sample to be translated a single time across the field-of-view at a fixed velocity, which provides additional constraints to the imaging system design, constraints that are more suited to conditions involving a piece of luggage moving across a conveyor belt rather than

for clinical applications [35]. Therefore, the flexibility in the CACSSI design makes it better suited for application in a clinical system than SICSI. As a result, CACSSI is the snapshot imaging technique that will be investigated in this dissertation. Next we discuss the simulation tool that we use for preliminary investigations into these imaging systems.

1.4 Dissertation outline

Chapter 2 of this thesis will focus on developing an accurate MC simulation that incorporates coherent scattering physics for use in subsequent chapters for the development of coherent scatter imaging. In that chapter we also present validation of the simulation using experimentally acquired data.

Chapters 3 and 4 The following two chapters will focus on developing and optimizing CSCT and CACSSI imaging systems using MC simulations for cancerous voxel classification.

Chapter 5 will focus on testing the optimized imaging systems for intra-operative margin detection through virtual clinical trials. The virtual clinical trials comprised generating a population of realistic virtual tissue samples and imaging them using MC simulations and analyzing the results using receiver-operator characteristics (ROC) statistical analysis.

Chapter 6 will focus on imaging a cancerous breast tissue specimen in experiment using coherent scatter imaging and validate the imaging results using tissue histology as a form of validation of the MC simulations in the preceding chapters. This dissertation provides the medical imaging community with a CSCT and coded aperture imaging design that can effectively distinguish cancerous tissue in realistic homogeneous distributions of breast tissue for intra-operative margin detection and that can be adapted to other breast cancer imaging applications such as mammography.

2

Development and validation of a Monte Carlo (MC) simulation for coherent scatter imaging

Parts of the work presented in this chapter were published in Nuclear Instruments and Methods in Physics Research, Section B, 335: 31-38, 2014 [12].

In this chapter, we describe the development and validation of an MC simulation for accurate modeling of coherent scatter physics. The accuracy of this simulation that we were able to demonstrate in this chapter allows us to proceed with using MC simulations for developing the coherent scatter imaging systems in subsequent chapters.

2.1 Introduction

In this study, we use Monte Carlo (MC) simulations in addition to experimental work to investigate coherent scatter imaging systems. MC simulations take into account sources of noise and artifacts that are present in an experimental scenario, such as x-ray source and detector-related effects, statistical noise associated with the detection process, and realistic physics interactions such as Compton scattering,

multiple scattering and self-attenuation. The key difference between MC simulations and experiments is that necessary experimental apparatus such as x-ray detectors and x-ray sources and the tissue sample itself can be modeled virtually, without any resource limitations associated with equipment setup and geometry, making this an attractive approach for preliminary investigations.

Currently, none of the commonly used MC codes for radiation transport, e.g., GEANT4 [72, 73], PENELOPE [74, 75], or MCPNX [76, 77] model the interference of coherent scattered photons in diffraction that would allow one to image the molecular structure of the sample. Coherent scatter diffraction is not modeled in most MC simulations for two reasons: First, the interatomic spacing or configuration of atoms in the materials is not a single default value; and second, in many MC codes such as GEANT4, photons are tracked one at a time in the simulation, so interference between photons or electromagnetic waves cannot be modeled readily. Therefore, developing a MC simulation that can accurately model coherent scattering is a significant part of this dissertation. This chapter describes the development of such a simulation in GEANT4 for use in subsequent sections of the research.

We choose to use the GEANT4 [72] MC toolkit because we have used it in the past for the development of medical imaging systems [78, 79], we have validated its electromagnetic physics against experiment [80, 81], and it is open source, making it possible for us to make the modifications discussed in this chapter. GEANT4 models coherent and incoherent scattering using re-engineered implementations of the PENELOPE MC code [74, 75].

The models for both types of scattering use the independent atomic approximation (IAA) for scattering [82], which neglects interference between electromagnetic waves scattering off of electrons or atoms near each other in a medium. The IAA is used in MC simulations because the inherent structure of MC simulations is incompatible with how electromagnetic interference needs to be modeled, which is the

case for two reasons: (a) MC simulations inherently track photons one at a time and independent of each other, whereas electromagnetic interference involves interactions between different photons; and (b) MC simulations model materials based on their density and atomic composition, whereas the modeling of electromagnetic interference involves the spatial structure. While the IAA is accurate for radiation scattered through large angles, it breaks down for small angles at which diffraction is most observable. Coherent scatter radiation is most intense in this small-angle range.

Other MC packages such as EGSnrc [83] allow the user to provide and specify the angular distribution for coherent scatter diffraction for materials. While the ability is useful, successful modeling of the angular distribution requires that it be known precisely for a given material–either through experimental measurement, or obtained from the literature if it has already been measured.

The lack of diffraction modeling in the coherent scattering implementations of MC simulations is typically ignored in most studies for three reasons: first, the cross section for coherent scattering is smaller (usually by at least an order of magnitude) than the cross sections for incoherent scattering; second, there once existed the misconception that diffraction effects only occurred for the case of crystals (i.e., Bragg diffraction) and not for amorphous materials; and finally, because diffraction patterns are not so easily observed for non-collimated (e.g., parallel- or cone- beam) geometries that are most often used in radiographic x-ray imaging [82].

A number of simulation studies have focused on quantifying the effects of coherent scatter diffraction signals as noise in x-ray radiography measurements [84–87] and for using coherent scatter in diagnosing breast cancer [88–90]. However, as a result of the limited resources for the simulation of coherent scatter diffraction, no studies prior to ours have simulated an x-ray scatter imaging system. We have done so by modifying the source code in Geant4 to accurately model coherent scattering as

detailed in Section 2.2.

2.2 Methods

In this section we first describe the development of the coherent scatter MC simulation and then how it was validated experimentally.

2.2.1 Implementation of Diffraction Modeling in GEANT4

The GEANT4 implementation for coherent scattering models the angular distribution of coherent scattered x-rays using the following equation [74]:

$$\Phi(E,\theta) = FF^2(q)(1+\cos^2\theta)\sin\theta\ , \tag{2.1}$$

where $FF(q)$ is the form factor, which is equal to the Fourier transform of the electron charge distribution in the scatterer [59]; q is the momentum transfer, which is related to the scatter angle θ and the x-ray energy E through $q = (E/hc)\sin(\theta/2)$; and h and c are Planck's constant and the speed of light in vacuum, respectively.

GEANT4 and PENELOPE use the form factors for coherent scatter based on individual atoms (e.g., absent interference effects) from EPDL97 [91] (EPDL Evaluated Photon Data Library, 1997 version), which are the non-relativistic values calculated by Hubbell [92]. Therefore, implementation of coherent scatter diffraction modeling in GEANT4 requires enabling the simulation to use form factors representative of the entire material (i.e., with interference effects taken into account) in place of those for individual atoms in the execution of Eq. (2.1) during the course of the simulation.

Hence, we modified the GEANT4 physics code for Rayleigh scattering to utilize the form factors in the GEANT4 data directory based on the material involved in the photon interactions within a compound rather than based on the individual atoms involved. Examples of the simulated differential coherent scatter cross sections before

and after modifying the physics of the simulation to utilize form factors from experimental measurements instead of the IAA has been shown in [82] for lucite, water and nylon. The authors show that the IAA gives curves that are broad and slowly varying, whereas the more realistic form factors that incorporate electromagnetic interference have more high frequency peaks and structures, which is what makes XRD and coherent scattering useful for material identification. In addition, we developed a database of form factors for various materials (measured experimentally as described next) to include into the GEANT4 data directory that the simulation can access at run time for execution of Eq. (2.1).

We measured the form factors for various materials using a Panalytical XPert PRO HR x-ray diffraction (XRD) system (see Fig. 2.1) with a 1.8-kW sealed ceramic x-ray source and a Ni 0.125-mm automatic beam attenuator. Incident beam optics also included $\frac{1}{2}^{\circ}$ fixed divergence slit and 10-mm mask to define the beam dimension. The diffracted beam optics included Soller slits to limit axial divergence (0.04 rad) and a parallel plate collimator with a 0.27 acceptance angle. X-rays were measured using a sealed proportional detector with 84% efficiency for Cu kα. Samples were $\sim$4 mm in thickness, secured onto the measurement stage for analysis, as shown in Fig. 2.1, and measured in reflection mode. Scattering angles from 2° to 120° were scanned with a step size of 0.05° and 0.5 s time per step. The diffraction system introduced an intensity spike at q-values near zero due to measurement of the unattenuated primary incident beam that needed to be removed as a post-processing step.

2.2.2 Validation of MC simulation against experiment

Next, the experimental data to use for validation of the MC simulation was acquired using our CACSSI experimental setup that we describe in Section 6.2.1, and for which the MC simulations we describe in Section 4.2.1. However, instead of breast

(a) Sample (b) Diffraction System

FIGURE 2.1: Figures showing the (a) sample and (b) Panalytical XPert PRO HR diffraction system used for measuring the form factors. The sample has been secured onto the measurement stage of the diffraction system for analysis in (b).

samples, validation is performed using three simple targets materials placed inside a 10-mm vial: (1) table salt (i.e., NaCl), (2) aluminum and (3) polyester.

After the coherent scatter data are acquired–measured as a function of E and θ–from the experiment and MC simulation, the data are used to reconstruct the sample form factor–which is a function of momentum transfer q. The form factor is then directly compared to the form factor measured using the XRD system described in the previous subsection. The reconstruction was performed using the CACSSI reconstruction algorithm described in Section 4.2.2. The match between the experimental and simulation data was evaluated by calculating the Pearson's linear correlation coefficient between the two.

2.3 Results

Comparison of the reconstructed form factors between XRD, experiment and the MC simulation are shown in Fig. 2.2. The XRD data is included in the figure order to demonstrate how the various differences between the XRD system and the CACSSI imaging system affect the reconstructed form factor. The differences in the

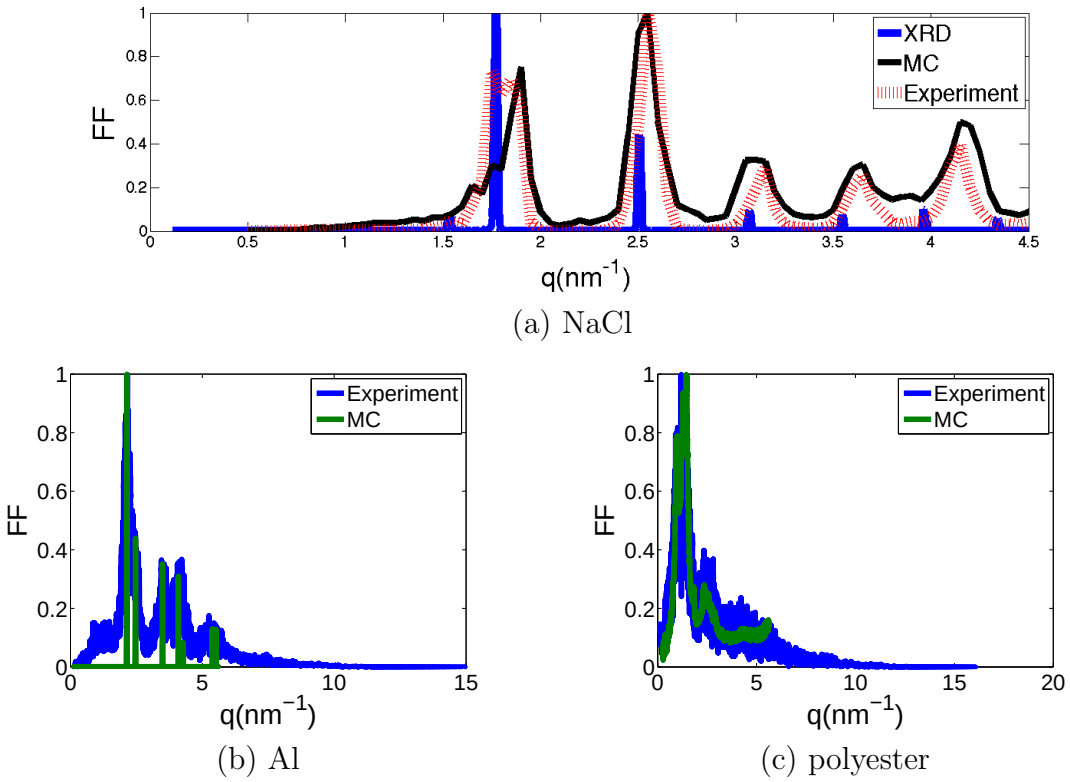

(a) NaCl

(b) Al

(c) polyester

FIGURE 2.2: Results of the reconstructed form factor for (a) table salt, (b) aluminum and (c) polyester from XRD measurements, MC simulations and experimental measurements. The match between the MC simulation and the experiment validates the accuracy of the MC simulation.

reconstructions between the XRD and CACSSI results (i.e., the MC simulation and the experiment) are caused by the less fine precision in the CACSSI system: the greater thickness of the samples that were used, the broader energy spectrum in the incident x-ray beam, and the larger pixel sizes in the detector. The excellent match (correlation coefficient of 0.84) between the MC simulations and the experiments–especially in contrast to the XRD results–serves to validate the MC simulations.

2.4 Discussion

The correlation coefficient between the reconstructed form factors from experimental and simulation being 0.84 instead of unity is likely caused by a combination of (a)

differences between the actual and simulated incident x-ray spectrum, (b) scattering off of the pinhole collimators in the experiment, and (c) the electronics in the photon counting detector.

The simulated incident spectrum was generated using the XSPECT software [93–95] based on the known x-ray tube anode material, filtering and voltage used in the experiment. However, the actual energy spectrum of the x-ray produced from the tube could differ from that generated using XSPECT due to the aging of the tube which could cause a decrease in the quality of the generated x-ray beam and changes in its energy spectrum and intensity.

The pinhole collimators used in the experiment are also known to generate scatter which would not be present in the MC simulation because in the simulation the pencil beam was simulated directly instead of through pinhole collimation. Finally, the x-ray pulse-height spectrum produced in photon counting detectors using finite-element and MC modeling of the crystals themselves is an area of active research [96]. Therefore our simplified modeling of the photon counting detector as only having (a) some spatial binning and (b) a Gaussian energy response will cause some disagreements between the MC and experimental results.

2.5 Conclusion

Despite the minor differences between the MC and experiment, the strength of the match between the two in Fig. 2.2 allows us to use MC simulation to model the coherent scatter imaging systems in the rest of this dissertation with a high degree of confidence that the conclusions we draw from the simulations can be extrapolated to an experimental setting.

3

Coherent scatter computed tomography (CSCT) imaging of cancer in resected breast tissue: a Monte Carlo study

The work presented in this chapter was published in the Proceedings of the SPIE 2014 Medical Imaging, 9033 [97] and in Physics in Medicine and Biology, 60(16): 63355, 2015 [11].

The following chapter describes a tumor margin assessment method based on X-ray coherent scatter computed tomography (CSCT) imaging and demonstrate its utility in surgical margin assessment using Monte Carlo simulations. The resulting volume-rendered images were found to distinguish cancerous tumors embedded in complex distributions of adipose and fibroglandular breast tissue (as is expected in the breast). The images exhibited sufficient spatial and spectral (i.e., momentum transfer) resolution to classify the tissue in any given voxel as healthy or cancerous. ROC analysis of the classification accuracy revealed an area under the curve (AUC) of up to 0.97. These results indicate that coherent scatter imaging is promising as a possible fast and accurate surgical margin assessment technique.

3.1 CSCT Implementation & Reconstruction

CSCT differs from conventional transmission CT in one key way – instead of the transmitted X-rays being detected and reconstructed to form an image as in conventional CT, the CSCT method relies on scattered X-rays to generate images. The concept was introduced in [98], in which CSCT was implemented based on a first-generation conventional CT scanner setup: a pencil beam of X-rays was translated and rotated relative to the sample with one modification to the standard CT setup to enable measurement of the scattered X-rays at specific scattering angles. A similar scanner setup was envisioned in our work.

In CSCT, the number of scattered X-rays N_s is measured at angle θ with energy E. Let $\triangle\Omega(\theta)$ be the solid angle subtended by the pixels at angle θ, and N_t be the number of transmitted X-rays measured at energy E. Using the inverse radon transform $\mathcal{R}^{-1}\{\}$, we can reconstruct a cross-sectional image of the product of the electron density $n_0(x, y)$ of the sample and the differential coherent scatter cross section $d\sigma_{coh}/d\Omega$ of the sample as [98]:

$$\mathcal{R}^{-1}\left\{\frac{N_s(\theta, E)}{\triangle\Omega(\theta)N_t(E)}\right\} \approx n_0(x, y)\frac{d\sigma_{coh}[x, y, q(\theta, E)]}{d\Omega} \ . \tag{3.1}$$

On the right-hand side of Eq. (3.1), $d\sigma_{coh}/d\Omega$ for a given point (x, y) in the sample depends on the momentum transfer, q. The momentum transfer is defined in terms of the incident X-ray energy E and the scatter angle θ: $q \equiv E\sin(\theta/2)/hc$. The differential coherent scatter cross section $d\sigma_{coh}/d\Omega$, which is a function of q, is proportional to the form factor, which we discussed in Chapter 1 has been shown to be significantly and reproducibly different for the different breast tissues.

3.2 Methods

The modeling of this study consisted of three components: (a) the modeling of the CSCT imaging system in the Monte Carlo simulation, (b) the classification technique used to identify the type of tissue in a given voxel in the reconstructed CSCT images, and (c) the strategy used to study the optimum imaging system parameters.

3.2.1 Modeling of the Coherent Scatter CT Imaging System

A coherent scatter CT imaging system and the breast tissue phantoms were modeled in Monte Carlo simulations in order to determine whether CSCT was feasible for imaging surgically-removed breast tissue. The Monte Carlo simulations were run on a computer cluster of 300 parallel processors using a technique for distribution developed in our group [99], which resulted in a 3-hour per 100 mAs run time for the case of a 0.75-mm pencil beam. The modeling included four individual components to be modeled: (a) the X-ray source, (b) the X-ray detector, (c) the breast tissue phantom, and (d) the CT gantry.

As we discussed in Section 2.2.1, the form factors for each material in the simulation has to be defined ahead of time. To do so here, we used the form factors measured *ex vivo* for adipose, fibroglandular, normal, and cancerous tissues taken from [1], [50], [51], [47], and [2].

X-ray source

The X-ray source was modeled as a collimated pencil-beam of X-rays (shown as a horizontal green line across the middle of Fig. 3.1) with a realistic energy spectrum. The energies of the X-rays were modeled using the MASMIP [100] code to resemble a mammography X-ray tube manufactured by Eureka X-ray Tube, Inc.. The tube was assumed to have a molybdenum anode, with 40 kV applied tube voltage and 0.5 mm beryllium filtration from the X-ray tube window and no added filtration. The source

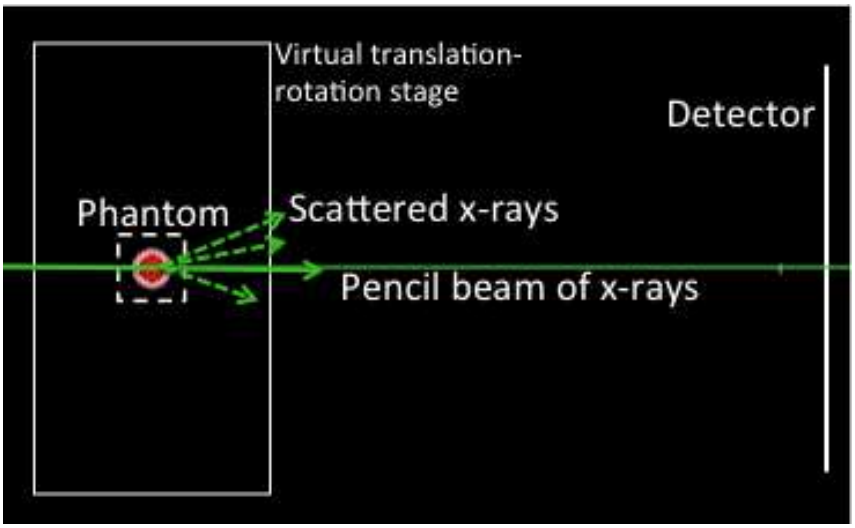

FIGURE 3.1: Shown is the coherent scatter CT imaging system modeled in this work, made up of four components labeled in the figure: 1) pencil-beam of X-rays; 2) planar X-ray detector; 3) breast tissue phantom; and 4) virtual CT gantry.

was kept stationary for the entire scan while the sample was translated and rotated through the beam to acquire the CT projection data.

X-ray detector

The detector position, energy-resolution, and spatial-resolution were modeled to resemble our experimental system described in Section 6.2.1. The detector was modeled as a flat rectangular detector (shown as the vertical white line at the far right-hand side of Fig. 3.1) with physical dimensions of 30 cm×40 cm divided into a two-dimensional pixel array of 384×512 of 0.78 mm pixels. The pixels were modeled to be energy sensitive with typical 6 keV energy resolution. The detector crystal material as it relates to quantum efficiency was modeled without the physical properties of any specific material; instead, it was modeled to report photon flux with perfect efficiency.

The detector was placed 50 cm from the breast tissue sample. The breast tissue sample and the center of the detector were both aligned with the pencil-beam. Due

to this alignment, the central pixel of the detector counted the X-rays transmitted through the sample (N_t), whereas the remaining surrounding pixels counted the scattered X-rays (N_s).

Breast tissue phantom

This study aims to evaluate the technology, using realistically-shaped breast tumors embedded in heterogeneous healthy breast tissue. To do so, the breast tissue phantoms [9] were formed by cropping out a 2.7-cm cube of voxels from a realistic virtual anthropomorphic breast phantom. The virtual breast phantom was built by segmenting five classes of healthy breast tissue from high-resolution CT images of healthy patients. The segmentation was performed by first denoising the images using a 3D anisotropic diffusion algorithm, then applying histogram thresholding to produce initial gland and skin segmentations, and finally applying a novel glandular linking and extension protocol based on a skeletonization of the skin and glandular segmentations [101]. This approach has been shown to mimic realistic breast phantoms in previous studies [9]. Realistic mathematically modeled breast cancer lesions based on lesions segmented from high resolution tomosynthesis images [102] were then inserted into these cubes of healthy breast tissue. Single slices of the virtual anthropomorphic phantoms are shown in Fig. 3.2(a) and (f), and volume renderings of the cancerous tumors in the virtual phantoms are shown in Fig. 3.3(a) and (c).

The elemental compositions (e.g., % hydrogen, % carbon makeup) of the adipose, fibroglandular, normal and cancerous breast tissues were modeled from literature [103] reporting the composition of 46 human female breast tumors and healthy samples (measured through *in vivo* neutron activation analysis). The densities of adipose, fibroglandular and cancerous tissues were modeled as $0.93\,\mathrm{g/cm^3}$, $1.04\,\mathrm{g/cm^3}$, and $1.058\,\mathrm{g/cm^3}$, respectively, based on values commonly used in Monte Carlo modeling of breast tissue [104].

Virtual CT gantry

The virtual CT gantry was modeled to impart translation and rotation to the phantom. It can be seen in Fig. 3.1 as the large rectangle, with solid white lines at its boundaries containing the breast tissue phantom. The stage "moves" the breast tissue phantom through the pencil beam in a series of horizontal and vertical translations, as well as rotations.

For all scans in this work, each tomographic slice in the sample was acquired using 20 projection angles; 44 translation steps of the pencil beam at each angle; and 20 tomographic slices or heights in the sample. The tomographic field-of-view (FOV) or cross-sectional view for a single tomographic slice is shown in Fig. 3.1 as the small square with white dotted lines.

3.2.2 Tissue Classification in CSCT Images

A surgical margin detection technique must provide appropriate information for clinicians to identify whether sufficient healthy tissue margins exist around the tumor. A margin detection technique should ideally delineate the spatial distributions of healthy and cancerous tissue in the sample in 3D. Consequently, we sought to identify the presence of cancerous tissue in the CSCT images based on pixel intensities. This ability to identify whether a given voxel is cancerous is the most useful feature of CSCT. Here we describe the technique used in this work to classify the tissue in each voxel of the CSCT image as being either cancerous or healthy.

Pixel intensity as a function of momentum transfer q can be used to identify the type of tissue. As shown in Eq. (3.1), the pixel intensity in CSCT is equal to the differential coherent scatter cross section ($d\sigma_{coh}/d\Omega$) multiplied by the electron density n_0. Out of these two factors, only the differential coherent scatter cross section depends on momentum transfer; the electron density does not depend on momentum transfer. Therefore, if we vary momentum transfer, the intensity of a given pixel in

the reconstructed CSCT image is directly proportional to the differential coherent scatter cross section. Recall that the differential coherent scatter cross sections significantly differ between adipose, fibroglandular, normal and cancerous tissue (Sec. 1.2). Therefore, since pixel intensity is proportional to differential coherent scatter cross section, the pixel intensity can be used to determine whether the tissue at that pixel is adipose, fibroglandular, normal or cancerous.

CSCT images as a function of q can be reconstructed by forming separate sinograms for each combination of the two variables upon which q depends: scatter angle θ and detected X-ray energy E. Summing over all sinograms for a given q value and reconstructing using Eq. (3.1) provides the CSCT image with that q value. For the image reconstruction operation $\mathcal{R}^{-1}\{\}$ in Eq. (3.1), we used the inverse radon transform function with the Ram-Lak filter in MATLAB [105]. We choose the Ram-Lak filter because the image reconstructions are being performed in the spatial domain where the data is less susceptible to noise and where it is desirable to preserve high frequency features for margin detection. There is noise present in CSCT images, but it is more prevalent in the signal as a function of momentum transfer or q. Because the image reconstruction is performed independently for each q-value, the choice of reconstruction filter would have no bearing on the noise in the signal as a function q.

Each voxel in the reconstructed 3D CSCT image was classified based on its intensity as a function of q. Voxels that exhibited orders of magnitude lower integrated intensity than the other voxels in the image were classified as being air or empty space. Otherwise, the voxel intensity curve was normalized to unity, and a binary classifier was applied to determine whether the voxel contains cancerous tissue or non-cancerous tissue. The binary classifier first computed the Euclidean (i.e., straight line) distance–as a metric of separation or difference in a higher dimensional space–between the voxel intensity curve and the $d\sigma_{coh}/d\Omega$ curve expected for cancerous

tissue by subtracting one curve from the other and then computing the l^2-norm of the resulting vector. The classification decision was then made based on whether the computed Euclidean distance is greater than some threshold value. That threshold value of Euclidean distance for binary classification can be treated as a variable decision criteria as in receiver operator characteristics (ROC) analysis [106]. Therefore, ROC analysis can be used to quantify the performance of the system as will be described in Section 3.2.3.

3.2.3 Optimization of Tomographic Acquisition Parameters

Here we describe how various imaging system parameters were varied with the resulting effects on image quality observed using a set of metrics. The method for varying the imaging system parameters are described first, followed by a description of the image quality metrics.

Parameters for Optimization

As described in Section 3.2.1, a collimated pencil beam was used to scan the sample. Because the scan is performed using a finite number of projection angles and beam steps, the choice of these two tomographic sampling rates (i.e., the angular and spatial sampling rates) is critical to the resulting quality of the reconstructed image. Specifically, the spatial sampling rate determines the voxel size of the reconstructed image. Because the total scan time and X-ray tube heating are proportional to the number of projection angles and beam steps used, time limitations and tube-current limitations can impose constraints on the tomographic sampling rates that can be used. In addition, the incident X-ray tube mAs (i.e., the X-ray tube current-product) used at each position must be carefully chosen in order to obtain sufficient signal given time and tube-current limitations. In order to optimize these three parameters (angular sampling rate, voxel size, and mAs), we performed a series of scans varying

each parameter one at a time in order to observe its effects on image quality.

Increasing the voxel size was achieved by increasing the pencil beam width and stepping the wider beam through fewer steps so that the effective illumination of the FOV was maintained constant. For example, if we double the beam width, the number of beam steps would be reduced by a factor of two so that the spacing between adjacent beams would be doubled. The X-ray tube mAs used for the double-width beam would be maintained identical to the thinner beam so that the X-ray fluence (i.e., X-ray exposure per unit area) would be constant regardless of the voxel size.

Image Quality Metrics

For a given CSCT image, the voxels in the image were classified as cancerous if the Euclidean distance of their reconstructed $d\sigma_{coh}/d\Omega$ intensity curves from the expected curve for cancerous tissue was greater than a pre-determined threshold value, which we choose using the method described in the next paragraph. For a given threshold value, we can compare the resulting classified image when using that threshold value to the ground truth. From that comparison, we can compute the true and false positive rates of the classification as well as the true and false negative rates. From these rates, the sensitivity and specificity can be computed.

However, the sensitivity and specificity, and therefore the overall accuracy, depends on large part on how we choose the pre-determined threshold value. Consequently, we choose to use ROC analysis here because it allows us to treat the pre-determined threshold value as a variable decision criterion. Namely, ROC analysis allows us to test the diagnostic efficacy of our imaging systems independent of how we choose this threshold value. By varying the threshold value, the plot of sensitivity versus $(1 - \text{specificity})$ provides the ROC curve for the voxel classifier, from which the AUC was computed by integrating. The AUC represents the coherent imaging system's inherent ability to discriminate between cancerous and healthy voxels, or

the probability that a randomly chosen cancerous voxel is rated or ranked as more likely to be cancerous than a randomly chosen healthy voxel. As a result, the first metric used for assessment of image quality was the area under the curve (AUC) from the ROC analysis.

A second metric of a modulation transfer function (MTF) [107] was also computed, representing the degree to which objects of varying frequencies are detected by an imaging system. We determined the MTF by scanning a cube of graphite of side-length 12 cm tilted 5.5° counter-clockwise in the imaging plane relative to the imaging system axes. This technique of imaging a tilted edge, detailed in [108], allows one to sample the edge spread function (ESF) at a much greater sampling frequency and considerably reduced noise than when imaging a straight edge. The curve-fitting technique introduced in [109] was applied to compute the LSF and subsequently the MTF from the ESF. Recall that in CSCT, separate spatial images are reconstructed as a function of momentum transfer q. Therefore, the procedure for computing the MTF in CSCT differs from that for conventional x-ray CT in that here we choose to compute the MTF only for the reconstructed image corresponding to the q-value where graphite has maximum signal intensity. We choose that q value that gives the maximum signal intensity in order to reduce the effects of statistical noise in the MTF calculations.

3.3 Results

In this section, the CSCT images of a single tomographic slice in the two cancerous breast tissue phantoms are first presented, along with the result of classifying the cancerous voxels. Volume renderings of the classified cancerous tumors inside of the tissue samples are also presented. For the optimization part of the study, the tissue classification AUC as well as the imaging system MTFs are presented for CSCT imaging systems with varying numbers of projection angles, voxel sizes and X-ray

tube mAs.

3.3.1 Tissue Classification in CSCT Images

2D Images

Figures 3.2(a) and (f) show the middle slices ($z = 0$) of the tissue phantoms with the following color scheme: pink for fibroglandular, red for normal tissue, blue for adipose and black for cancerous tissue. Figures 3.2(b), (d) and (g) show the reconstructed CSCT images for a fixed q value of $1.10\,\mathrm{nm}^{-1}$, where the difference in scatter intensity between cancerous and fibroglandular tissue is the greatest. The single-slice CSCT images shown in Fig. 3.2(b) and (g) were acquired using a 0.40 mm voxel size, 90 projection angles, and 27 mAs per pencil beam; and for comparison Fig. 3.2(d) was acquired using one-third the number of projection angles, or 30, in order to observe the effect on the reconstructed image quality and classification results. Finally, Fig. 3.2(c), (e) and (h) show the images after the pixels have been classified. The classifications shown are for using the Euclidean distance threshold for binary classification that gives the maximum pixel accuracy A_{max}. (The pixel accuracy A was defined as $A = (TP + TN)/N$, where TP is the number of true positive pixels, TN is the number of true negative pixels, and N is the total number of pixels in the image.) The performance of the imaging system for classifying voxels as cancerous can be assessed by comparing the tissue classifications in Fig. 3.2(c), (e) and (h) to the phantoms in Fig. 3.2(a) and (f).

3D Rendering of Tumor Volumes

Taking the classified cancerous tissue from all of the 2D CSCT slices provides the volume renderings of the reconstructed tumors (Fig. 3.3(b) and (d)). The volumetric images shown were acquired using a 0.40 mm pixel size, 90 projection angles, 27 mAs per pencil beam, and a 1.25 mm slice sampling rate. For comparison, the volume

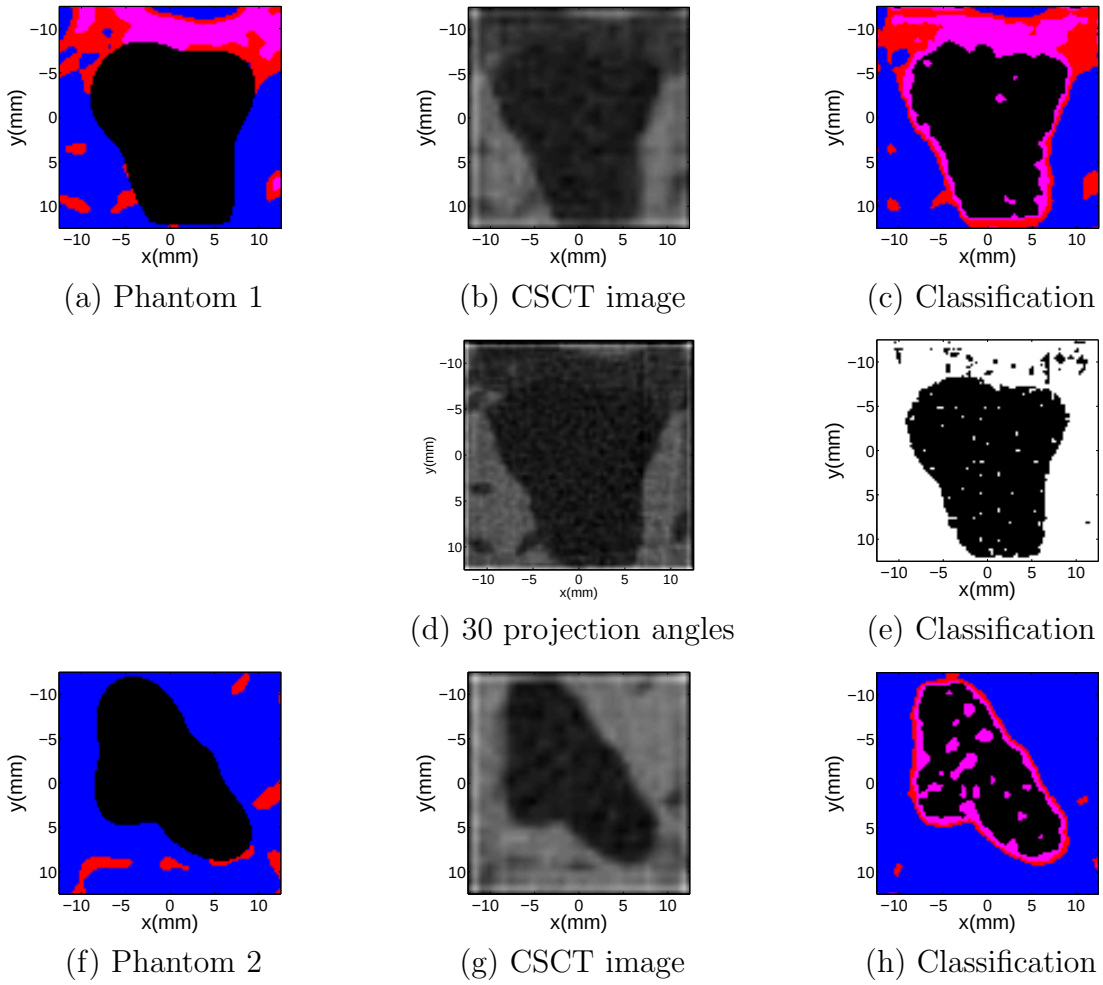

(a) Phantom 1 (b) CSCT image (c) Classification

(d) 30 projection angles (e) Classification

(f) Phantom 2 (g) CSCT image (h) Classification

FIGURE 3.2: The first column shows a single slice at $z = 0$ of the two virtual tissue phantoms that were placed inside of the imaging system. Pink represents fibroglandular tissue, red represents normal tissue, blue represents adipose and black represents cancerous tissue. The second column shows the reconstructed CSCT images of the slice in the two phantoms for a fixed q-value of $1.10\,\mathrm{nm}^{-1}$. The images in (b) and (g) were acquired using a 0.40 mm voxel size, 90 projection angles, and 27 mAs per pencil beam; whereas the image in (d) was acquired using one-third the number of project angles or 30. The third column shows the images from the second column after each pixel was automatically classified as being cancerous or healthy.

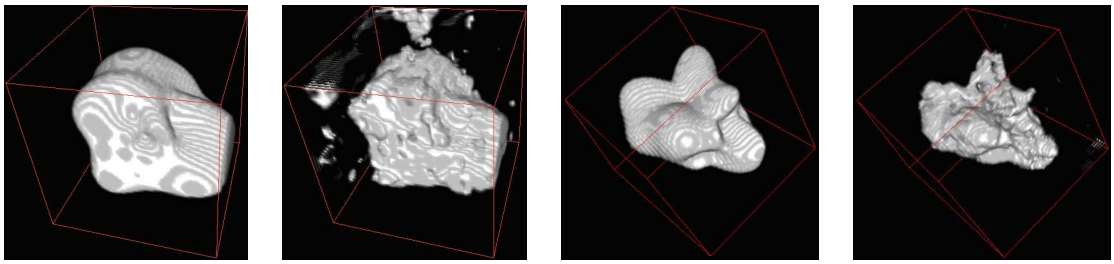

(a) Phantom 1 (b) Classification (c) Phantom 2 (d) Classification

FIGURE 3.3: Subfigures (a) and (c) show true volume renderings of the cancerous tissue inside of the virtual phantoms that were placed in the imaging system. Subfigures (b) and (d) show the volume renderings of the reconstructed classified tumors from CSCT. The resemblance of the reconstructed volumes from CSCT to the true tumors show that the CSCT imaging system has the potential to automatically classify the cancerous tissue inside of a sample. The scans were performed using a 0.40 mm pixel size, 90 projection angles, 27 mAs per pencil beam, and a 1.25 mm slice sampling rate.

renderings of the true cancerous tumors from the virtual tissue phantoms used for imaging are shown in Fig. 3.3(a) and (c). The boundaries of the tissue phantoms are represented by the green lines forming the cubes around the tumors in all four subfigures. The volume renderings of the reconstructed tumors from CSCT have shapes that generally resemble the original phantoms and demonstrate that the imaging system has the potential to automatically and accurately render breast tumor volumes embedded in heterogeneous healthy breast tissue.

3.3.2 Optimization of Tomographic Acquisition Parameters

The pixel classification AUC for Phantom 1 plotted against voxel size, number of projection angles, and X-ray tube mAs are shown in Fig. 3.4. The AUC of the highest performing CSCT imaging system in this work is 0.97. The MTFs for the imaging system for varying number of projection angles and voxel size is shown in Fig. 3.5. The interpretation of these results will be discussed next.

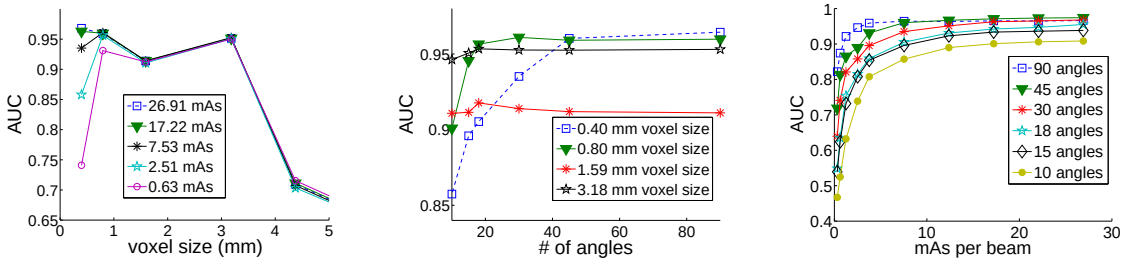

(a) voxel size (b) # of angles (c) tube current

FIGURE 3.4: Pixel classification AUC for Phantom 1 plotted against the (a) voxel size for various X-ray tube mAs and for 30 projection angles, (b) number of projection angles for various voxel sizes and 7.53 mAs per pencil beam, and (c) X-ray tube mAs per pencil beam for various numbers of projection angles and 0.40 mm voxel size.

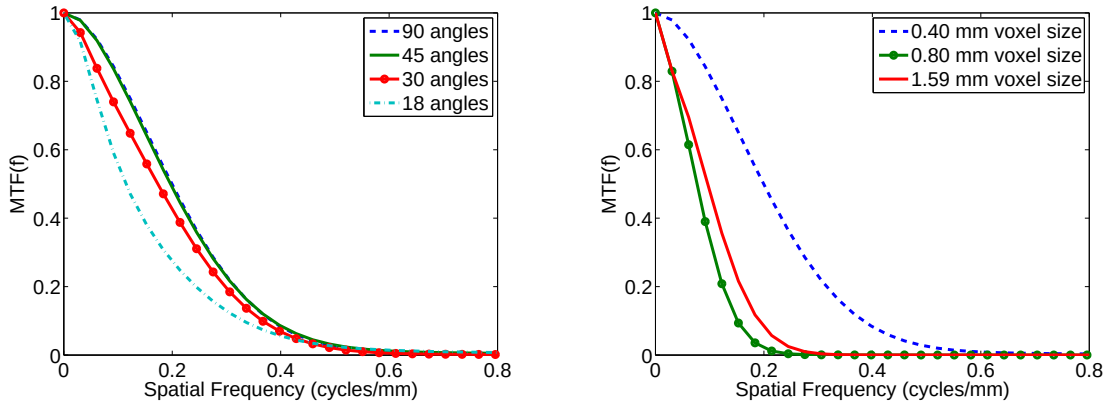

(a) MTFs using 0.4 mm voxel size (b) MTFs using 90 angles

FIGURE 3.5: MTFs for the CSCT imaging system when using different numbers of angles and voxel sizes for the tomographic acquisition.

3.4 Discussion

The imaging results shown in Fig. 3.2 and 3.3 show the potential of the CSCT imaging system in detecting and classifying malignancy in tissue. As mentioned before, the cancerous pixel classification shown in the third column of Fig. 3.2 were obtained by determining the Euclidean distance threshold of the binary classifier (i.e., the variable decision criteria) that gives the maximum classification accuracy and then

using that threshold for the binary classification. The volume renderings shown in Fig. 3.3 were also obtained using a Euclidean binary classifier whose threshold was selected in the same manner through optimization. In contrast, in a realistic diagnostic imaging scenario in which the ground truth image is unknown, the ability to obtain a pixel classification result as accurate as those shown in the third column of Fig. 3.2 and in Fig. 3.3(b) and (d) would depend on the judgment ability of the physician or technologist to manually select the classification threshold that gives the most reasonable result. The physician may instead choose the option of setting the threshold of the classifier so that the imaging system is more sensitive to cancerous tissue, at the expense of specificity.

Independent of the task of choosing the threshold value of the binary classifier, the proximity to unity of many of the AUC values shown in the plots in Fig. 3.4 reflect the potential robustness of the diagnostic performance of CSCT. Figure 3.4(a) shows that the diagnostic accuracy is dependent on the X-ray tube mAs for small voxels (up to 1.5 mm in this study), but the effect of mAs is reduced for voxels larger than 1.5 mm. Because the mAs increases proportionally with the number of projection angles, the effect on AUC of the number of projection angles is reduced for voxels larger than 1.5 mm as well. This result indicates that the diagnostic accuracy at the small voxel sizes is affected by the signal intensity, which may be insufficient when the voxel size is small. However, as expected, there is an optimal voxel size where the tradeoff between signal intensity and resolution is balanced to give the maximum AUC. From Fig. 3.4(b), we can see that the number of projection angles is important for the AUC mainly when the voxel size is small (less than 1.5 mm). As in the previous case (Fig. 3.4(a)), the accuracy of voxel classification for the smaller voxels is most likely limited by the signal-to-noise ratio, which increases with the greater X-ray exposure that accompanies taking projections at additional projection angles.

Specifically in Fig. 3.4(b), the curve for the 1.59 mm voxel size exhibits the lowest AUC values for greater than 30 projection angles. The imaging system used to generate the data in Fig. 3.4(b) used 7.53 mAs per pencil beam, and it can be seen in Fig. 3.4(a) that the curve for 7.53 mAs per pencil beam shows a local minimum at 1.59 mm voxel size. Therefore, the curve for the 1.59 mm voxel size exhibits the lowest AUC values. The three subfigures in Fig. 3.4 demonstrate the complex interdependency of the voxel size, x-ray tube mAs and the number of projection angles on the AUC of the system.

In both cases (Fig. 3.4(a) and 3.4(b)), voxel sizes of less than 1 mm show the highest variations in AUC and tube current. Therefore, when the AUC is plotted against X-ray tube mAs in Fig. 3.4(c), it is done for a fixed voxel size of 0.40 mm so that the variation in the AUC with X-ray tube mAs can be observed clearly. In that plot, we can see that even at 0.40 mm, increasing the X-ray tube current beyond 7.53 mAs per pencil beam gives little or no improvement in the AUC.

Figure 3.4(b) shows that 3.18 mm voxel size gives the maximum AUC across all angles. This information can be used to guide the design of a CSCT imaging system: A system designed for greatest detection accuracy should use the larger (3.18 mm) voxel size, whereas a CSCT system designed for best image resolution should use a smaller (0.40 mm) voxel size. Figure 3.5(a) shows that increasing the number of projection angles beyond 45 does not result in any substantial improvement in the MTF.

By delineating the presence of cancerous and healthy tissue throughout the surgically removed tissue section, CSCT can provide sufficient information for determining whether the removed tissue has positive or negative margins. However, one of the tumor renderings presented in this work misclassified a cluster of voxels near an edge of the tissue sample (see Fig. 3.3(b)), which could be interpreted as a true cluster of cancerous tissue (i.e., a false positive). While the rate of occurrences of such

misclassified voxels is low, the source of misclassification must be understood and eliminated, which is an ongoing effort in our group.

From Fig. 3.4, the AUC of the imaging system with optimum parameters is 0.97, demonstrating the potential of CSCT for automatic margin detection in breast surgery. The challenge for this imaging technique going forward is the scan time. In order to achieve an AUC above 0.9, one set of imaging parameters that could be used is 0.80 mm voxel size, 10 projection angles, and 7.53 mAs per beam (i.e., the least AUC data point in the 0.80 mm voxel (green triangle) curve in Fig. 3.4(b)). Assuming a typical mammography X-ray tube that generates X-rays at a rate of ∼100 mA, the time needed to generate 7.53 mAs for 10 projection angles and a 0.80 mm voxel size for the scanning of a single slice would be roughly half a minute. To scan an entire volume using 20 tomographic slices would therefore require 10 minutes. This duration may be somewhat long for a clinical surgical team to have to wait intra-operatively with an incised patient under anesthesia on the operating table, and therefore, we have begun [110] investigating compressive sensing techniques using coded apertures to potentially reduce the scan time to a few minutes [35, 71].

The simulations presented in this work did not model some effects that would occur in an experimental system such as the divergence of the beam and the energy-dependence of the detector efficiency. Experimentally, the beam divergence could be minimized by moving the source farther away from the pinhole collimator. The effect of the beam divergence would be that the beam width would be magnified at the phantom, causing a penumbra effect, which would result in a slight degradation in spatial resolution (to 1 mm instead of 0.40 mm achieved here). The energy-dependent detector efficiency would cause distortions in the reconstructed coherent scatter cross section as a function of q. However, these distortions are straightforward to correct by applying a weighting factor to the measured count data as a function of the x-ray energy based on the known energy-dependent efficiency of the detector crystal.

3.5 Conclusion

In this chapter, we demonstrated through Monte Carlo simulations that CSCT can potentially delineate healthy and cancerous tissue in surgically resected breast tissue specimens with an AUC up to 0.97. The results show the ability to identify the type of breast tissue in a given group of pixels in the CSCT images by plotting their intensity as a function of momentum transfer, and then matching the shape of the plotted curve to the known differential coherent scatter cross section of cancerous breast tissue.

The ability of a CSCT system to visually delineate healthy and cancerous tissue in small tissue samples suggests that CSCT is a promising technique for surgical margin detection that could be an effective aid to a surgical team during a BCS procedure. This work represents the first results from a CSCT investigation to detect margins in tumors excised through BCS.

4

Coded aperture coherent scatter spectral imaging (CACSSI) of cancer in resected breast tissue: a Monte Carlo study

Parts of the work presented in this chapter have been submitted for publication in the Journal of Medical Imaging [111].

In this chapter we describe the application of the coded aperture coherent scatter spectral imaging technique to reconstruct 3D images of breast tissue samples from Monte Carlo simulations. We first perform a quantitative assessment of the accuracy of the cancerous voxel classification of the imaging system and we then optimize the various parameters in the CACSSI imaging system. From the Monte Carlo simulation results, we find that coded aperture scatter imaging is able to reconstruct images of the samples and identify the distribution of cancerous and healthy tissues (i.e., fibroglandular, adipose, or a mix of the two) inside of them with a cancerous voxel identification sensitivity, specificity, accuracy and AUC of 92.4%, 91.9%, 92.0% and 0.94, respectively. These results show that coded aperture scatter imaging has the potential to provide scatter images that automatically differentiate cancerous and

healthy tissue inside of ex vivo samples within a time on the order of a minute per slice; and the optimization results provide us with an imaging system to use for the virtual clinical trials in the subsequent chapter.

4.1 Introduction

Coherent scatter computed tomography (CSCT) was successfully applied in the previous chapter to spatially delineate cancerous tissue within heterogeneous distributions of breast tissue. However, the pencil beam CSCT scans performed required the beam to be raster scanned along two axes and then rotated about the target object at multiple projection angles in order to generate a 3D image. This scanning approach makes it necessary to perform thousands of pencil beam acquisitions. This process is prohibitively time-consuming and difficult to implement experimentally with high precision, particularly when volumes as large as a breast or lung must be imaged. Moreover, X-ray tube heating coupled with the inefficiency of collimating the source to produce thin pencil beams makes it prohibitive to generate thousands of pencil beams in a clinical setting. Therefore, we explored an alternative method of generating 3D coherent scatter images without a need for tomographic rotation of the sample or of the imaging system.

Here we design and demonstrate the coded aperture coherent scatter spectral imaging (CACSSI) [71] technique for breast cancer imaging and detection. CACSSI uses a coded aperture placed in front of the detector to make multiplexed measurements of the scatter. When the coded aperture is placed in front of the X-ray detector, it spatially modulates the scattered X-rays by a frequency dependent on the location of the scatter origin. By identifying the origin of scatter along the pencil beam, the coded aperture enables reconstruction of images of the sample without any need for tomographic rotation.

To demonstrate the technique, we first performed a quantitative assessment of

the accuracy of the imaging system in Monte Carlo simulations. After imaging, the type of breast tissue in each voxel was identified by matching its reconstructed differential coherent scatter cross section $d\sigma_{coh}(q)/d\Omega$ to the known cross sections of different breast tissue types from literature. Finally, we perform an optimization of the various parameters in the CACSSI setup for the achievement of the highest possibly accuracy for cancerous voxel detection in surgically resected breast tissue specimens.

4.2 Methods

In this section, we first describe the Monte Carlo simulations used to model CACSSI, we then describe the coded aperture reconstruction algorithm, and finally we describe the design of the optimization of the CACSSI imaging parameters optimization that was performed.

4.2.1 Monte Carlo Modeling

As in the previous chapter, Monte Carlo simulations of the imaging system in this chapter were developed in GEANT4 [72]. The CACSSI imaging system modeled in the Monte Carlo simulations is identical to the experimental system described in Chapter 6. A visualization of the simulation of the CACSSI system is shown in Fig. 4.1. The setup comprised an X-ray source, a translation stage, a coded aperture, and a linear array of 128 energy-sensitive X-ray detector pixels. Each component of the system is described below.

Instead of modeling a point source followed by pinhole collimators as is the case in our experiment, we directly modeled a perfectly collimated pencil beam of X-rays (with diameter $w = 0.75\,\text{mm}$) in order to optimize total simulation time. The X-ray beam fluence was matched against experiment to ensure that this collimated beam model did not deviate from real-world physical results. The energy spectrum was

modeled using the XSPECT software [93, 94] to resemble the spectrum corresponding to the experimental X-ray tube (Varian Model G1593BI: rotating Tungsten-rhenium anode; focal spot size of 0.8 mm, 125 kVp and 50 mA).

In order to mimic the translation stage used in our experiment for imaging, the virtual simulated scan was performed by raster scanning the breast sample through the pencil beam along the x direction through a 28 mm field-of-view (FOV_x) in steps of 4 mm. An X-ray tube-current product of 290 mAs was used for each acquisition. The simulations were run using the same computer cluster and parallel process distribution technique that was used and described in Chapter 3. In addition, the breast tissue phantom from Chapter 3 was used again here (see Fig. 4.2(a)) and it was placed at $z_o = 677$ mm.

The resolution in z (i.e., parallel to the beam) was achieved using a test coded aperture. The coded aperture comprised a series of bars of bismuth-tin alloy that each has size 1 mm in width and 50 mm in height, and that were arranged in a repeating pattern with spatial frequency of $u = 0.5\,\mathrm{mm}^{-1}$. Therefore, the gap or spacing between each bar is 1 mm. The coded aperture was placed at $z_m = 782$ mm and the series of bars ran along the x direction, with the height of the bars oriented along the y direction.

Also, in order to optimize simulation time, the energy-sensitive detector array was modeled to have perfect efficiency, spatial and energy resolution. Then, as a post-processing step, the measured count data from the detector was spatially binned, binned in energy, and then blurred in energy. These post-processing steps were performed in order to model the energy-sensitive detector used in our experiment, which was a linear array of 128 square cadmium-telluride (CdTe) photon counting detectors (Multix ME-100 Version 2), with pixel size 780 μm and energy-resolution of 6.5 keV FWHM. The detector array was placed at $z_d = 865$ mm and the linear array was oriented along the x direction.

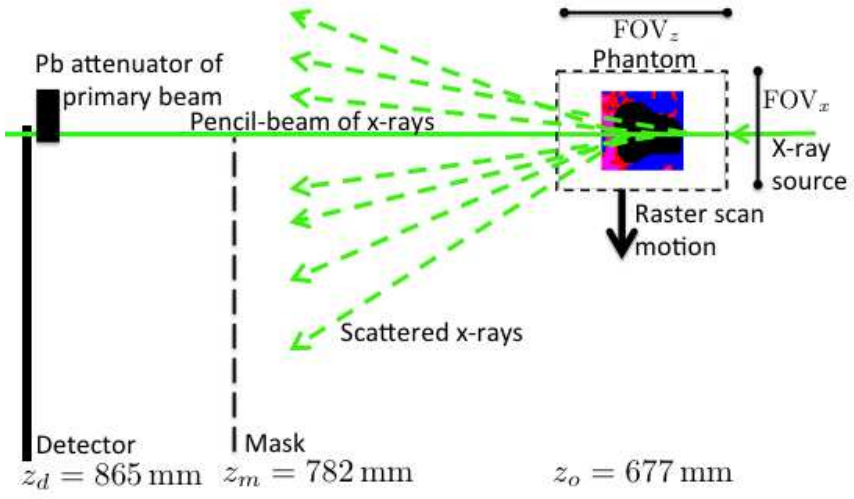

FIGURE 4.1: Visualization of the CACSSI system in the Monte Carlo simulation. The simulation was modeled based on the experimental setup from Chapter 6.

This imaging system could be engineered for clinical use by incorporating the various components into a compact scanner that can fit into an operating room. The distance between the sample and the detector can be seen from Fig. 4.1 as being less than 19 cm, which does not include the x-ray tube. Even after adding the size of an x-ray tube to the 19 cm needed to fit the components between and including the sample and the detector, the scanner would still be able to easily fit into an operating room.

4.2.2 Image reconstruction and tissue classification

The acquired data for each pencil beam acquisition were in the form of photon counts across the 128 pixels and 64 energy channels, as reported by the detector. The differential coherent scatter cross section ($d\sigma_{coh}(q,z)/d\Omega$) as a function of q (which is known as the momentum transfer) and z position (i.e., location along the pencil beam) were then reconstructed for each pencil beam acquisition using a maximum a posteriori (MAP) estimation method based on the algorithm developed in Ref. [112].

The reconstruction algorithm is a model-based iterative reconstruction technique: a matrix is formed that can be used through matrix multiplication as an operator to model the imaging system; then the algorithm iteratively determines the solution that best satisfies the matrix equation using the MAP estimate method to reach convergence. Using this reconstruction algorithm, each pencil beam acquisition was reconstructed separately and then finally combined to form the full image.

As mentioned previously in Sections 1.2.3 and 3.2.2, the relative coherent scatter intensity or the shape of the differential cross section ($d\sigma_{coh}(q)/d\Omega$) for a given pixel in the field-of-view as a function of momentum transfer q can be used to identify the type of breast tissue at that point in space. Therefore, once $d\sigma_{coh}(q)/d\Omega$ is reconstructed for each pixel along z in each of the pencil beam projections across the sample (in both x and y), the resulting voxels in the reconstructed 3D coded aperture scatter image can be classified to determine the corresponding tissue type: adipose, normal, fibroglandular, cancerous tissue (or there may no match) based on the shape of its $d\sigma_{coh}(q)/d\Omega$ function. Specifically here we classified each voxel in the 3D coded aperture scatter images based on a match of its coherent scatter pattern ($d\sigma_{coh}(q)/d\Omega$) with the scatter patterns from Kidane et al. [1] that were shown in Fig. 1.1. The match was performed by evaluating the correlation coefficient between the actual (Kidane) and measured (CACSSI) scatter patterns. If a given voxel showed a correlation coefficient below 0.8 (minimum threshold value), it was not classified as tissue and was instead classified as air or "nothing". Mixtures or cases of multiple tissue types within a single voxel were not explicitly considered in this work (other than normal tissue, which was described by Kidane et al. as a 50-50 mixture of adipose and fibroglandular tissue).

Because it is virtual, the ground truth phantom is known and can therefore be used for quantitative accuracy assessment of the imaging system. The ground truth phantom was sampled to match the sampling rate used in the reconstructed image,

and was then used to calculate the sensitivity (true classification rate of positive voxels), specificity (true classification rate of negative voxels), and accuracy of the imaging system for the detection of cancerous voxels.

4.2.3 Optimization of imaging parameters

The parameters we seek to optimize for the CACSSI imaging system are the pencil beam diameter, the coded aperture mask spatial frequency, the coded aperture mask location, the detector location, the x-ray tube and the x-ray tube current product (i.e., the tube mAs).

The generalized analytic theory for CACSSI spatial resolution and momentum transfer resolution presented in [71] shows that imaging performance–in terms of spatial and momentum transfer (i.e., q) resolution–improves with higher frequency mask features, smaller beam widths and with greater separation between the mask and the detector. Based on that analytic theory and the starting imaging system just described in the previous subsection, we hypothesize that the imaging system that will perform the best here is one with a $w = 0.5\,\text{mm}$ beam diameter, $1.33\,\text{mm}^{-1}$ mask feature size or period, $z_m = 750\,\text{mm}$ mask location, $z_d = 1200\,\text{mm}$ detector location, our 125 kVp WRe x-ray tube used in our experiments, and an x-ray tube current product comparable to the 290 mAs used in the first part of this chapter. From this proposed best case, we perturb each of the parameters to observe its effect on the overall imaging performance. The final set of imaging parameters that were tested are shown in Table 4.1.

For consistency, we choose to use the same objective metric for evaluation of each parameter-set that we used to optimize CSCT in Chapter 3: ROC analysis using the same binary classifier used in Chapter 3. It computed the Euclidean distance between the reconstructed voxel intensity curve and the known $d\sigma_{coh}/d\Omega$ curve for cancerous tissue. Then the classification decision was made based on whether the computed

Euclidean distance is greater than a predetermined threshold value, which is the variable decision criterion for the ROC analysis.

4.3 Results

The first step of this work was to use Monte Carlo simulations of the imaging system in order to evaluate its classification performance against a known ground truth. The classification results of the simulated coherent scatter images are shown in Fig. 4.2. Figure 4.2(a) shows the original phantom; Fig. 4.2(b) shows the ground truth image; and Fig. 4.2(c) shows the result of the classification process. The ground truth image in Fig. 4.2(b) is the original phantom, but subsampled based on the raster-scan step-size along x (4 mm) used in the image acquisition process. When we quantitatively assess the accuracy of the pixel classification–specifically for the task of detecting cancerous pixels–the classification image shown in Fig. 4.2(c) was found to have a sensitivity (i.e., the percentage of cancerous pixels that were correctly identified as being cancerous) of 92.4%, specificity (i.e., the percentage of healthy pixels correctly identified as healthy) of 91.9%, and accuracy for cancerous pixel detection of 92.0%. The 8% of pixels classified inaccurately were primarily attributed to spatial blurring due to the finite spatial resolution of the system along the z-direction (i.e., along beam propagation), Poisson noise and residual model error in the reconstruction. The spatial blurring along z leads to misclassification in two ways: (a) detection of signal in pixels where the object was not originally present, and (b) blending of the differential coherent scatter cross sections between neighboring pixels causing one or both of them to be misclassified. Despite this error margin, the imaging system demonstrated high classification accuracy (92%) for the classification of the 1000 voxels in the reconstructed image, strengthening the promise of the technique for experimental implementation.

The second phase of this work, after demonstrating the accuracy of the initial

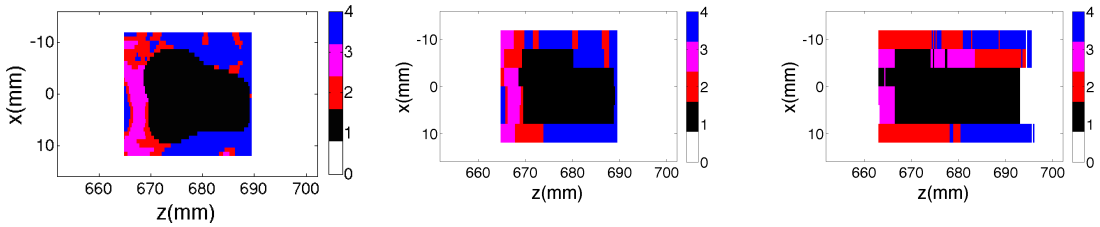

(a) Modeled phantom (b) Sampled phantom (c) Classification results

FIGURE 4.2: Comparison of the (c) classification results obtained for the reconstructed coherent scatter images from the Monte Carlo simulations with the (a) modeled phantom and the (b) sampled ground truth phantom. As in the other ground truth and classification figures in this dissertation, the color scheme used here is white (air), black (cancerous tissue), red (normal tissue), magenta (fibroglandular tissue), and blue (adipose tissue). The sensitivity, specificity and accuracy for classification of the cancerous pixels is 92.4%, 91.9%, and 92.0%, respectively, supporting the accuracy of the coherent scatter imaging technique for cancer imaging.

CACSSI setup, was to optimize the various parameters in the imaging system by evaluating the system AUC for cancerous voxel classification in the breast phantom, which provides a sample size of 1000 voxels. The resulting AUC values we obtain for the various imaging systems are shown in Table 4.1. The first row represents our hypothesized optimal imaging system, and in the following rows we indicate the parameters that were perturbed from the first row using bold-face font. The concluded best case imaging system (row 3) based on maximum AUC is indicated with a box around it and that imaging system will be used for the virtual clinical trials in the next chapter.

In order to understand how much signal is needed, we also show the AUC as a function of the x-ray tube current product for the top four performing imaging systems in Fig. 4.3.

Table 4.1: AUC values for various CACSSI imaging systems. As a short-hand, we only indicate the anode material in the "tube" column. The tube "WRe" represents the tungsten-rhenium anode tube used in our experiment and in the first phase of this chapter, whereas "Mo" represents the molybdenum mammography tube that we used in the CSCT simulations in the previous chapter. These AUC results were obtained from images acquired using an x-ray tube current product of 50 mAs per pencil beam (although the improvement in AUC for increasing mAs for the top four performing systems here is shown in Fig. 4.3). Row 1 was our expected best case imaging system based on analytic theory for best spatial and spectral resolution. Perturbations from Row 1 are indicated using bold-face font. The best imaging system (i.e., the one with maximum AUC)–that will be used for the virtual clinical trials in the next chapter–is indicated with a box around it.

#	w(mm)	u(mm^{-1})	z_m(mm)	z_d(mm)	tube	AUC
1	0.5	1.33	750	1200	WRe	0.81
2	**2.0**	1.33	750	1200	WRe	0.84
3	0.5	**0.50**	750	1200	WRe	0.92
4	0.5	1.33	**1000**	1200	WRe	0.67
5	0.5	1.33	750	**900**	WRe	0.81
6	0.5	1.33	750	1200	**Mo**	0.59
7	0.5	**0.50**	**1000**	1200	WRe	0.60

4.4 Discussion

In this section we discuss the long-term potential for CACSSI as well as comparisons of its imaging performance to that of CSCT that was found in the previous chapter.

4.4.1 Clinical applicability of CACSSI

The initial Monte Carlo assessment of the imaging system showed a cancer detection accuracy of 92.0% (Fig. 4.2) and AUC of 0.94 (Fig. 4.3). In a conventional transmission image, a radiologist must manually read the image and identify suspicious regions to detect cancer or other abnormalities. On the other hand, the coherent scatter images provide the differential coherent scatter cross section for every voxel in the sample that can be used as an identifying molecular signature of the tissue in that voxel, thereby enabling accurate and automatic classification (and subsequently detection) of the disease.

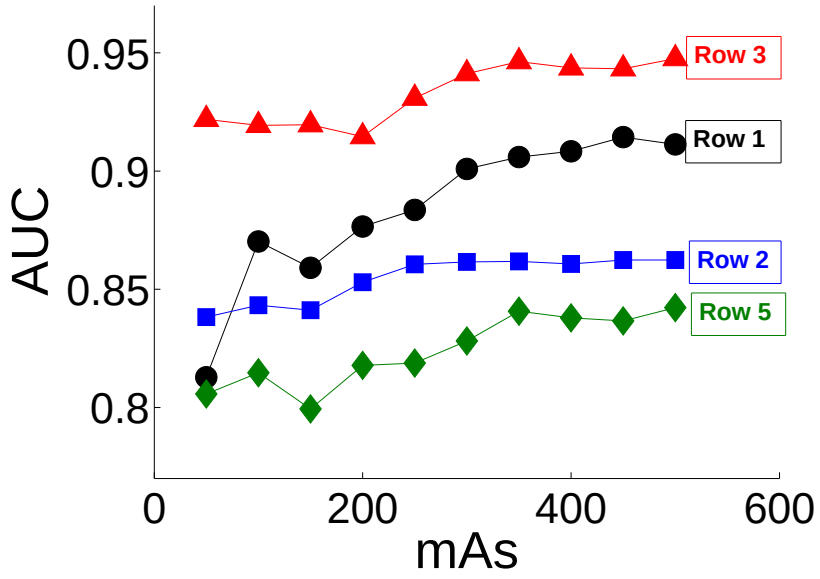

FIGURE 4.3: AUC versus x-ray tube current product for the top four performing imaging setups from Table 4.1. We can see that the top performing system only has a ∼3% improvement in AUC when the tube current product is increased from 50 to 500 mAs. Therefore, we will use 50 mAs for the scans in the virtual clinical trials in the next chapter to minimize scan time.

The coded aperture scatter imaging technique described in this chapter was able to map out the distribution of cancerous breast tissue in the specimen using a single-angle imaging approach (i.e., without any tomographic rotation of the sample or of the imaging system). This approach results in reduced dose and short scan-durations, making it appealing for both ex vivo and in vivo analyses in clinical settings.

The results of this work also support the use of coherent scatter imaging for in vivo applications where the path-length of the beam through the object is less than ∼3 cm (i.e., the sizes of the tissue samples imaged here). Based on our other investigations using thicker objects [12], the imaging system can be optimized to image thicker objects such as compressed breasts typically imaged through mammography. These findings suggest that coherent scatter imaging could potentially evolve as a

standalone diagnostic tool or serve as a complementary tool to mammography for breast cancer detection.

4.4.2 Initial comparisons to CSCT

Scan time

The necessary scan time for CACSSI is much shorter than that required for CSCT. For example, the results shown in Fig. 4.3 show that the top performing imaging system ("Row 3"), only has a ∼3% improvement in AUC performance accompanying an increase in mAs from 50 to 500 mAs. Therefore, we will proceed with using 50 mAs for the CACSSI scans in the virtual clinical trials in the next chapter. Experimentally, a 50 mAs scan which would result in a scan time of 8 seconds to acquire the entire slice shown in Fig. 4.2(c) using an X-ray tube operating at 50 mA (as was used in our experiments in Chapter 6). Whereas we showed in the previous chapter that CSCT requires half a minute per slice when using a 2D 512×384 detector array rather than the linear-detector array of 128 pixels used here. Therefore, when using the same detector array, CACSSI would be at least an order of magnitude faster than CSCT.

Accuracy

However, the maximum CACSSI AUC we observed here was ∼0.94 (Fig. 4.3), whereas we showed that CSCT can obtain an AUC of 0.97 in the previous chapter. The reduced AUC for CACSSI is due to its poorer spatial resolution than CSCT. The spatial resolution along the beam (z) direction determined in the initial Monte Carlo results (Fig. 4.2) in this chapter for CACSSI was ∼2.5 mm (whereas the spatial resolution along the x and y directions is the beam width, which was 0.75 mm).

However, when we tried to improve the spatial resolution by using a higher frequency coded aperture mask in the optimization part of the study, we found that the lower frequency coded aperture masks gave better AUC (Table 4.1). The worse

imaging results when using the higher frequency coded aperture masks is most likely caused by the noise in the system. When the reconstruction algorithm does not model the noise in the system accurately enough, the noise in the system can then result in artifacts in the reconstructed image. These artifacts are more prevalent when using a higher frequency coded aperture mask because the signal from the breast specimen in that case is higher frequency due to the modulation from the coded aperture mask and therefore it becomes more difficult to separate the true signal from the noise because the noise is also high frequency.

4.5 Conclusion

Using Monte Carlo simulations, we demonstrated that CACSSI can achieve a cancer detection accuracy of 92.0% and an AUC of 0.94. Coded aperture scatter imaging can generate volumetric images without the need for tomographic rotation of the sample, and it can map the distribution of different types of breast tissue in the sample automatically (as opposed to requiring a human reader). Therefore, it could serve as an effective tool for analyzing breast tissue samples in a clinical context in the future.

We were also able to show that CACSSI provides at least an order of magnitude shorter scan times than CSCT. However, the maximum CACSSI AUC value (0.94) is ∼5% lower than that obtained for CSCT (0.97) in Chapter 3. The optimized CACSSI imaging system found in this chapter will be used for the virtual clinical trials in the next chapter.

5

Virtual clinical trials evaluation of CSCT and CACSSI

In this chapter we perform clinical trials in Monte Carlo simulations in order to demonstrate the ability of CSCT and CACSSI to accurately perform the task of intra-operative margin detection. Evaluating the performance of the two imaging systems using ROC analysis, we find that CSCT and CACSSI give AUC values of 0.975 and 0.741, respectively, for accurately classifying breast cancer margins. Given the wide-ranging sensitivity and specificity values reported the currently used intra-operative margin detections, frozen section analysis and touch-prep cytology, that was discussed in Chapter 1, these AUC values for coherent scatter imaging show that it has potential to improve the clinical standard of care. In addition, these AUC values show that the diagnostic performance of CSCT is far superior to CACSSI.

5.1 Introduction

In the previous chapters we developed and demonstrated the accuracy of CSCT and CACSSI for cancerous voxel detection inside of breast tissue specimens. However, the goal of this dissertation is to develop coherent scatter imaging for the clinical

task of margin detection. Therefore, we must study the ability of CSCT and CACSSI to accurately classify the margins of breast tissue specimens.

Given this need to (1) study coherent scatter imaging for consistency over a range of cases, and (2) study the ability of coherent scatter imaging to accurately classify margins, in this chapter we perform "virtual clinical trials" (i.e., clinical trials in Monte Carlo simulations) of the two technologies for the clinical application of margin detection. Clinical trials are medical research studies that are performed on a group of human participants in order to test new treatments or medical devices through generating data on their efficacy. Therefore, this chapter is such a research study, performed virtually, in order to test the efficacy of coherent scatter imaging for the chosen clinical application.

5.2 Methods

In this section we describe the steps taken to generate the beast tissue specimen population, the imaging systems designs, the classifier algorithm that makes the clinical decision based on on the imaging results, and the ROC statistical analysis performed on the final results.

5.2.1 Generation of patient population

Specimens in the population were generated as follows:

1. a 30-mm cubic region of tissue (see Fig. 5.1(a)) was cropped from a random location inside of one of the realistic healthy XCAT breast phantoms from [9], which were formed by segmenting cone-beam CT images of the breasts of healthy women.

2. The external boundary of the specimen was generated by taking a unit sphere and perturbing the radial distance of all of the points on its surface by a

Gaussian random number with an average of 0 and standard deviation of 0.1. (The shape of surgically excised breast specimens has not been studied before. Therefore our purpose here is simply to generate a random shape for the excised specimen rather than modeling its exterior as a cube as was done in Chapters 3 and 4).

3. The perturbed spherical shape was then scaled in size to have a volume of $7.8\,\mathrm{cm}^3$ and used to mask the cube of healthy tissue to give it a realistic shape (see Fig. 5.1(b)). The specimen volume of $7.8\,\mathrm{cm}^3$ was estimated by assuming a sphere with a radius equal to the sum of the average observed tumor radius of 0.96 cm (based on a twenty-four thousand patient population from [113]) and the typical margin width or rim of healthy tissue around the tumor of $\sim$2.7 mm [114].

4. A realistic tumor (see Fig. 5.1(c)) was generated using a mathematical lesion model developed by [102].

5. The tumor was scaled to have a size that depended on whether the specimen was intended to have positive or negative margins. For positive margins, the tumor was scaled in size until it made first contact with the boundary of the healthy tissue volume at some point on its surface. For negative margins, the tumor was scaled in size so that the smallest distance between the tumor edge and the boundary of the healthy tissue volume met a pre-defined margin width value, determined as a random number uniformly distributed between 1 and 3 mm. This margin width was chosen based on the 2.7 mm average margin width from [114].

6. Finally, the scaled tumor was inserted into the healthy tissue sample to generate the final breast specimen (see Fig. 5.1(d)).

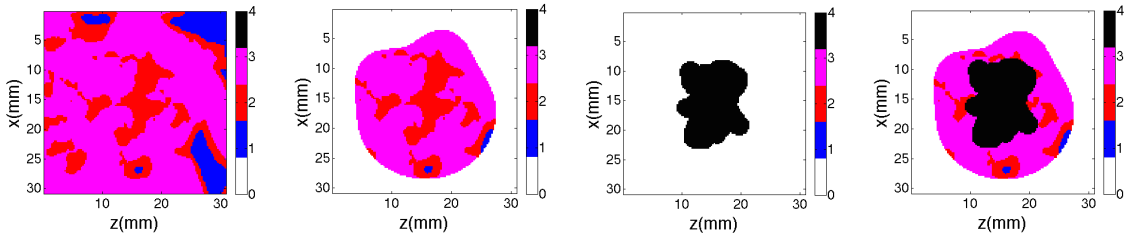

(a) Step 1 (b) Step 2 (c) Step 3 (d) Step 4

FIGURE 5.1: Images of the process used to randomly generate cancerous breast specimens. (a) Section of healthy tissue cropped from a segmented cone beam CT image of a healthy patient from [9]. (b) Realistic tumor generated using mathematical lesion from [10]. (c) The cancerous breast specimen generated by adding the lesion into the healthy breast tissue image. Color scheme: magenta - fibroglandular, blue - adipose, red - 50/50 fibroglandular/adipose mix, black - cancerous.

This six-step process was automated to generate a population of 92 specimens (see Fig. 5.2 for a sampling), which was the sample size that our ROC statistical analysis required as we discuss next.

Sample size determination

The minimum sample size required for the study was calculated so that the virtual clinical trials would generate ROC curves with power of 80% and a confidence interval of 95% for a width or margin of error of ± 0.1. To determine the sample size, we performed two pilot studies–one for CSCT and one for CACSSI–using 20 negative and 20 positive specimens (total: 40). Using the AUC values calculated for each of the two studies, the final sample sizes was calculated based on the width of a confidence interval for the AUC statistic of an ROC curve determined from [115]. The minimum sample sizes were then used to determine how many specimens would be imaged in the virtual clinical trials for CSCT and CACSSI, respectively.

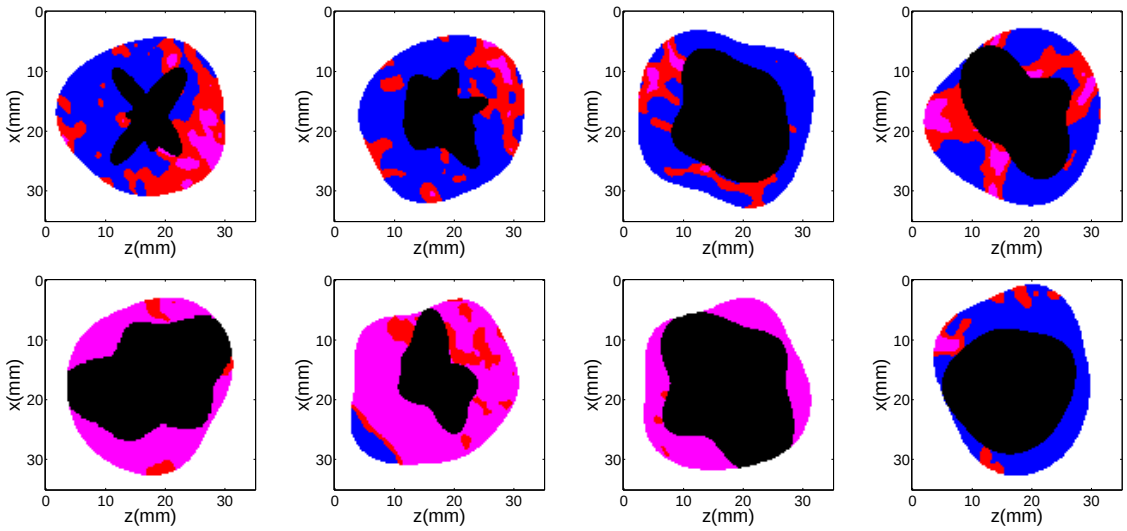

FIGURE 5.2: A sampling of the breast specimens used in this work in order to demonstrate the population diversity. The color scheme used here matches that used in Fig. 5.1. The first three specimens on the first row have negative margins. The last specimen on the first row and all specimens on the second row have positive margins.

5.2.2 CSCT & CACSSI imaging systems

The CSCT imaging system modeled in this work is based on the optimal imaging system determined in the optimization study in Chapter 3. From Fig. 3.4, which shows how the imaging system performs as a function of various CSCT imaging parameters, we determine that the cancerous voxel classification accuracy has diminishing improvement beyond a tomographic sampling of 45 total projection angles (i.e., a 4° sampling rate), 0.8 mm voxel size (i.e., 44 pencil beam samples at each angle across the 3.5 cm field-of-view), and 7.53 mAs tube current-product per pencil beam. Therefore, we use that optimal set of parameters for the CSCT imaging system tested in these virtual clinical trials: 45 projection angles, 0.8 mm voxel size, and 7.53 mAs per pencil beam.

The CACSSI system used in the virtual clinical trials is based on the optimal system found in Chapter 4. In that chapter, we found that the system with the

highest cancerous voxel classification accuracy has a 0.5 mm pencil beam diameter, $0.5\,\mathrm{mm}^{-1}$ mask spatial frequency, a mask location of 750 mm, detector location of 1200 mm, and an x-ray tube with a W-Re anode, operating at 125 kVp. Because we also saw in that chapter that the accuracy only improves by ∼3% when the x-ray tube current product is increased from 50 to 500 mAs, we use 50 mAs for the CACSSI imaging simulations in this chapter.

5.2.3 Classifier algorithm

After every sample is imaged, it was classified as either having positive or negative margins based on the reconstructed image. The specimen classification process can be broken down into two parts: (a) classification of each voxel in the image as cancerous or not–which is done using the same algorithm as was used in the previous two chapters–and then (b) classification of the entire specimen as having either positive or negative margins.

The first part of the classification process, which is cancer-detection on a voxel-by-voxel basis, was done using the same steps as in Chapters 3 and 4:

1. the Euclidean distance (i.e., the l^2-norm) is calculated between the reconstructed differential coherent scatter cross section of each voxel in the image and the known cross section behavior of cancerous breast tissue.

2. the voxels in the image that have a Euclidean distance that is less than a certain pre-determined threshold value are identified as being cancerous. The pre-determined threshold value is used as the variable decision criterion for the ROC analysis.

Once the voxels have been classified as cancerous or healthy based on the variable decision criterion, the second part of the classifier–which is the classification of the specimen as having either positive or negative margins–is done as follows:

1. the level-set segmentation algorithm–from [116] and [117]–was applied to the coherent scatter intensity image (i.e., the resulting image after integration of the scatter counts over all momentum transfer values) in order to determine the boundary of the specimen.

2. All voxels in the image outside this boundary are labeled as being 'air'.

3. We loop through all of the voxels in the specimen that were classified as cancerous and determine the distances from a given cancerous voxel to all air voxels surrounding the specimen, in order to determine how close the cancerous voxel is to a point on the specimen boundary.

4. We used the distances of all cancerous voxels to the specimen boundary to determine the smallest distance between any cancerous voxel and the specimen boundary.

5. Finally, we determine whether this smallest distance between a cancerous voxel and the specimen boundary is less than 1.6 mm–in which case the specimen is classified as positive–or whether it is greater than 1.6 mm–in which case the specimen is classified as negative.

The distance threshold of 1.6 mm corresponds to the distance covered by two voxels in our reconstructed image. Therefore, any distance determined to be less than 1.6 mm would indicate that some cancerous voxel is at the specimen boundary. This condition is the necessary grounds for positive margin classification based on the Society of Surgical Oncology (SSO) and American Society for Radiation Oncology (ASTRO) consensus [118] released last year. The consensus was written by a multidisciplinary expert panel called the Margins Panel convened by SSO and ASTRO for the purpose of determining what margin width minimizes the risk of breast cancer recurrence. The panel made the recommendation to the clinical community that

there are no benefits to having surgical margin widths greater than what is known as "no ink on tumor". The "no ink on tumor" terminology refers to the case that as long as the tumor is not at the surface of the specimen, which is the part that gets inked in pathology processing, that means that there is a sufficient margin of healthy tissue around the tumor. Therefore, as long as the tumor is not at the surface of the specimen, the specimen can be treated as having a negative margin.

5.2.4 Statistical analysis

The Euclidean distance threshold value is used as the variable decision criterion for the ROC statistical analysis of coherent scatter imaging systems and for making the binary decision of margin classification. Note that the ground truth margin classifications were known for all specimens because they were tracked during the generation of the population described in Section 5.2.1. Using the ground truth margin classifications, we calculated the sensitivity and specificity of the imaging systems for different variable decision criterion values.

From the sensitivity and specificity values, we plot the ROC curves for the CSCT and CACSSI systems and calculate the AUC. The AUC metric in this study represents the coherent imaging system's inherent ability to discriminate between positive and negative margin populations, or the probability that a randomly chosen positive margin case from some lumpectomy procedure is rated or ranked as more likely to be positive than a randomly chosen negative margin case [119].

5.3 Results

Examples of the imaging results from the CSCT and CACSSI systems are shown in Fig. 5.3. The first column shows the ground truth phantom. The second column shows the reconstructed coherent scatter images for a fixed momentum transfer value of $0.1\,\mathrm{nm}^{-1}$, i.e., where the contrast between healthy and cancerous tissue is the

Table 5.1: Final AUC values for CSCT and CACSSI imaging systems.

Imaging system	AUC
CSCT	0.975
CACSSI	0.741

greatest. The third column shows the classified image for the case of the variable decision criterion value for which the margin detection accuracy was greatest across the entire specimen population (the accuracy was computed as part of the ROC analysis as a function of variable decision criterion values). The ROC curves for the two imaging systems across the entire specimen population are shown in Fig. 5.4 and the corresponding AUC values for the two curves are shown in Table 5.1. The pilot study results for CSCT and CACSSI revealed that the minimum required population sizes were 26 and 92 specimens, respectively, which was used for the ROC results reported here.

5.4 Discussion

The AUC represents the imaging system's inherent ability to discriminate between positive and negative margin populations. Therefore, the AUC values obtained in this work for CSCT and CACSSI of 0.975 and 0.741 show that coherent scatter imaging is a promising technique to replace existing techniques such as frozen section analysis (FSA) and touch-prep cytology, which we discussed in Chapter 1 to have wide-ranging values for reported sensitivity (65 to 91% and 38 to 100%, respectively) and for specificity (86 to 100% and 85 to 100%, respectively). In addition, the much greater AUC for CSCT shows that its diagnostic performance is superior than that of CACSSI.

The greater AUC value for CSCT than CACSSI is largely due to its finer spatial resolution. The difference in AUC between CSCT and CACSSI is much greater in this chapter, for the task of intra-operative margin detection, than in Chapters 3

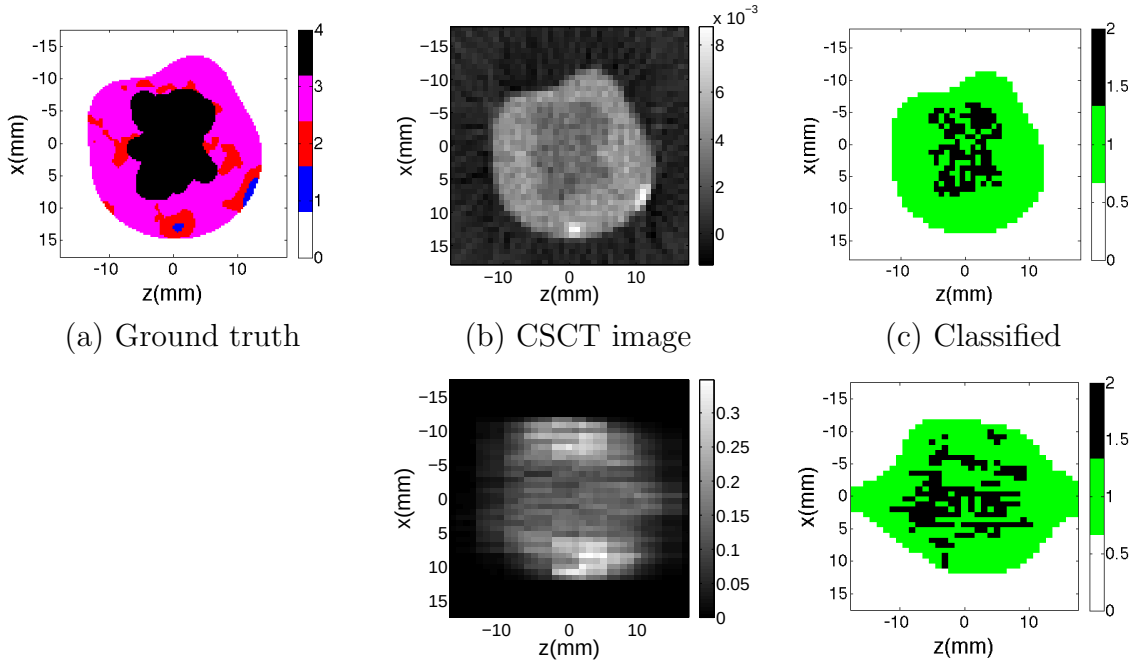

(a) Ground truth (b) CSCT image (c) Classified

(d) CACSSI image (e) Classified

FIGURE 5.3: Examples of the images and voxel classification. The classification is for using the variable decision criterion value that gave the highest margin classification accuracy over the entire population. Specifically shown are (a) the ground truth phantom, where, as in Fig. 5.1, white represents air, blue represents adipose tissue, red represents mixtures of adipose and fibroglandular tissues, magenta represents fibroglandular tissue, and black represents cancerous tissue; (b) the reconstructed CSCT image at the momentum transfer value $1.1\,\mathrm{nm}^{-1}$, which is where the scatter intensity for cancerous tissue is most different from other healthy breast tissues; (c) the classified image, using the threshold value that gave the highest accuracy for margin classification over the entire population, where white represents air, green represents healthy breast tissue, and black represents cancerous tissue; (d) the reconstructed CACSSI image; and (e) the classified image, again, using the same threshold value that gave the highest margin classification accuracy over the entire population and the same color scheme as used in (c). The ground truth phantom had a minimum margin size of 2.0 mm from the boundary at (11.25 mm, 6.5 mm), the CSCT classification result gives a margin width of 3.2 mm and the CACSSI classification result gives a positive margin.

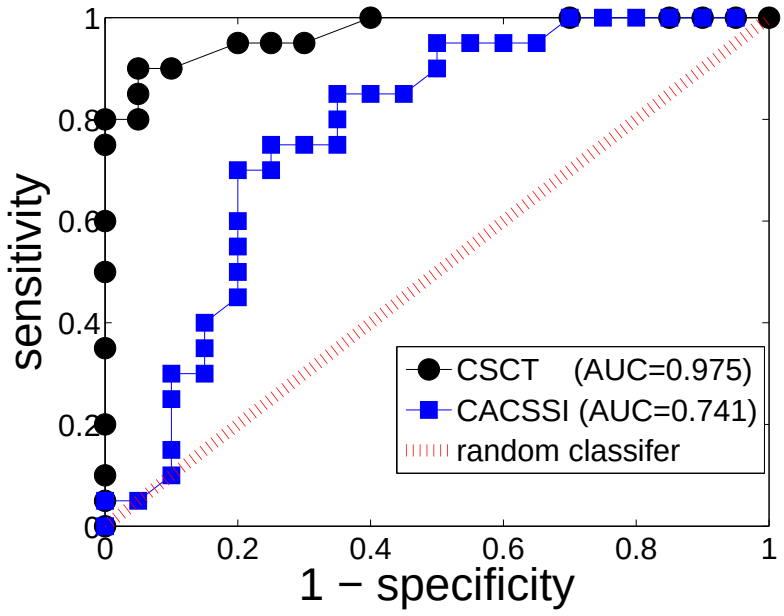

FIGURE 5.4: ROC curves for CSCT and CACSSI imaging systems for margin detection among the population of specimens used in this work. The AUC values for the two curves are 0.975 and 0.741, respectively.

and 4, where the task was individual voxel classification, because spatial resolution is much more important for margin detection than for classifying individual voxels. For margin detection, the ability to accurately detect a single point where a tumor makes contact with a specimen boundary is highly dependent on the imaging system's ability to image with fine resolution. Whereas the ability to classify a given voxel within the field of view may in fact actually worsen with improved spatial resolution since smaller voxels provide less signal. Since the many projection angles in CSCT allow it to have much finer spatial resolution than CACSSI, CSCT outperforms CACSSI to a much greater extent for margin detection. In contrast, for the task of voxel classification, which we studied in Chapters 3 and 4, CACSSI performs nearly as well as CSCT (only a 5% difference between the two in AUC).

However, because CACSSI does not require the 45 rotation angles that CSCT required in this work, its scan time is 45 times less than that for CSCT. As discussed

at the end of Chapter 4, the scan time for CACSSI would be on the order of 8 seconds per slice, or just under 3 minutes per volumetric scan. Therefore CSCT, which would take on the order of a magnitude more time to scan, would require just under about half an hour for a volumetric scan. Therefore, developing CACSSI to have a finer spatial resolution for improved diagnostic accuracy is worthwhile in order to take advantage of its reduced scan time.

The classification results in Fig. 5.3 show that the CSCT system is able to accurately classify most of the cancerous voxels. In this case, the most important cancerous voxels for detection are those closest to the specimen boundary. However, if we were looking to optimize the cancerous tumor classification or segmentation, a smoothing algorithm could be used to improve the match between the black classified voxels in Fig. 5.3(c) and the ground truth tumor in Fig. 5.3(a).

5.5 Conclusion

In this work we showed that coherent scatter imaging is able to perform effectively for margin detection in lumpectomy specimens across a diverse range of specimens. Specifically CSCT and CACSSI were shown to have AUC's of 0.975 and 0.741, respectively. These AUC values show that coherent scatter imaging has the potential to provide more accurate BCS margin detection than the currently used techniques in clinical practice of FSA and touch-prep cytology. Now that we have demonstrated the efficacy of coherent scatter imaging virtually over the last three chapters, we proceed to implement coherent scatter imaging experimentally in the next chapter.

6

Experimental validation of CACSSI for imaging cancerous breast tissue using tissue histology

Parts of the work presented in this chapter were published in the Proceedings of the SPIE 2015 Medical Imaging, 9412:94121F [120], have been submitted for publication in the Journal of Medical Imaging [111], and will be published in the Proceedings of the SPIE 2016 Medical Imaging [121].

In this chapter we present results from an experimental implementation of CACSSI and the validation of these results with tissue histology. The results show that the technique is able to identify cancerous and healthy tissue samples and reconstruct differential coherent scatter cross sections that are highly correlated with those measured by other groups using X-ray diffraction. In addition the validation with tissue histology shows that CACSSI is able to accurately identify cancerous breast tissue.

6.1 Introduction

In prior chapters we have demonstrated the efficacy of coherent scatter imaging for the task of margin detection, which was the goal of this dissertation. However, all of

the data that has been presented thus far has been from Monte Carlo simulations. An experimental implementation of coherent scatter imaging that has been shown to accurately detect breast cancer does not exist. Therefore, in this final research study of this dissertation, we experimentally implement coherent scatter imaging and test its ability to accurately detect cancer in a human breast tissue sample.

Thus far, we have developed and evaluated both CSCT and CACSSI. The AUC value for the task of individual voxel classification (i.e., from Chapters 3 and 4) is ∼5% lower for CACSSI than CSCT. The AUC value for the task of intra-operative margin detection (i.e., from the virtual clinical trials in the previous chapter) is ∼24% lower for CACSSI than CSCT. However, the scan time required for CSCT (on the order of 30 minutes for a volumetric scan) is ∼900% greater than that for CACSSI (on the order of 3 minutes). If a team of clinicians must wait for half an hour in the operating room for a coherent scatter image to be acquired, the technology would not be adding nearly as much value to the standard of care as if the scan could be acquired within 3-5 minutes. Therefore, the CACSSI technique has greater potential to impact healthcare with additional development. Consequently, we focus on the CACSSI technique in this chapter.

6.2 Methods

In this section we describe the CACSSI experimental setup and breast tissue samples used, how the images were reconstructed and processed, and the tissue histology and registration with CACSSI.

6.2.1 Experimental setup, data acquisition & breast tissue samples

The experimental setup (based on Ref. [71]) comprised an X-ray tube, two pinhole collimators, a coded aperture, and a linear array of 128 energy-sensitive X-ray detector pixels (see Fig. 6.1). Each component of the system is described below.

The X-ray tube is identical to the one modeled and described in CACSSI simulation from Chapter 4. The X-rays were collimated to a pencil beam of diameter 0.75 mm at the detector with angular divergence of ∼1 mrad using a two-stage collimator. In the first stage, a pair of 1 mm slits was used to collimate the beam to 1 mm × 1 mm cross section. Then, in the second stage, a 3 mm thick lead sheet with a 0.75 mm diameter circular hole was used to further collimate the beam to 0.75 mm diameter circular cross section. The beam spatial profile was verified using a higher spatial-resolution detector, specifically a stationary amorphous silicon indirect cesium iodide (CsI) flat panel energy-integrating detector (Paxscan, 4030 CB series, Varian Medical Systems) with a pixel size of 194 μm. The coded aperture was constructed from a 1 mm slab of bismuth-tin alloy machined into a series of uniform slits (see Fig. 6.1(b)). Each of the slits measuring 1 mm×1 mm×50 mm (width × thickness × height).

Three breast samples were used in this study. The samples were surgically excised from the human breast: the first was a healthy tissue sample and the second, a matched tumor excised from the same patient (see Fig. 6.2(a)). The third sample was a cancerous specimen from a different patient. All three samples weighed approximately 40 g and were roughly 2.5 cm in size. Each breast specimen was placed in the beam separately (see Fig. 6.5(a)) and scanned using a raster scanning method in x (i.e., across the table, perpendicular to the beam) and y (i.e., height above the table, perpendicular to the beam) using a computer-controlled translation stage for precise translation of the sample. A total field of view of (30 mm, 15 mm) (x, y) was imaged as follows. The sample was placed in the beam at its first location and scanned for 10 seconds with an X-ray tube current of 50 mA. The sample was then translated in x by 2.5 mm and scanned again. This process was repeated enough times to cover a roughly 30-mm field-of-view (or raster scan) in x for reconstruction of a cross-sectional slice of an x-z plane though the sample. The height (i.e., the y

coordinate) of the translation stage was then translated by 2.5 mm and the raster scan in x was repeated. Repetitions of 2.5-mm translations in y with raster scans in x were performed until a 15 mm field-of-view in y was covered in order to reconstruct volumetric images of the samples.

All remaining specifications for the experimental CACSSI system match those used in the CACSSI simulations in Chapter 4.

6.2.2 Image reconstruction & tissue classification

The x-ray scatter data per energy channel per pixel for each pencil beam acquisition was reconstructed using the reconstruction algorithm used for the CACSSI simulations (Chapter 4). Following reconstruction, each voxel was classified as being one of the four breast-tissue types using a similar algorithm that was used in the first part of Chapter 4. However, one modification to classification algorithm was made here.

Due to the large (5-mm) voxel size relative to the feature sizes of spiculated breast lesions, the possibility of multiple breast tissue types co-existing within a voxel was considered and accounted. Because the different breast tissues have roughly the same density and effective atomic number, and therefore roughly the same intensity of coherent scattering, the signal from a voxel containing two types of breast tissue is typically the superposition of the cross sections for the tissues involved. This effect is analogous to partial volume averaging in computed tomography. Therefore, the resulting signal will show the peak characteristics of the component tissue-types at relative intensities proportional to the ratio of the differing tissues comprising the scanned voxel. As a result, if a voxel was identified as having multiple peaks, we classified it as a mixture of the tissues that were known to exhibit those peaks.

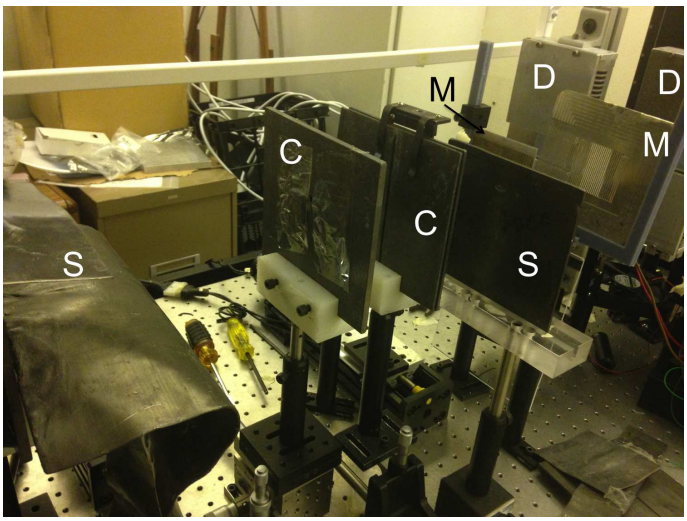

(a) Experimental setup

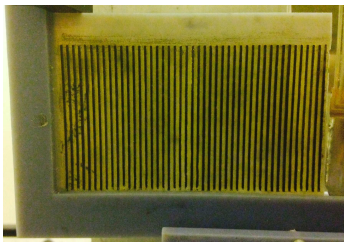

(b) Coded aperture

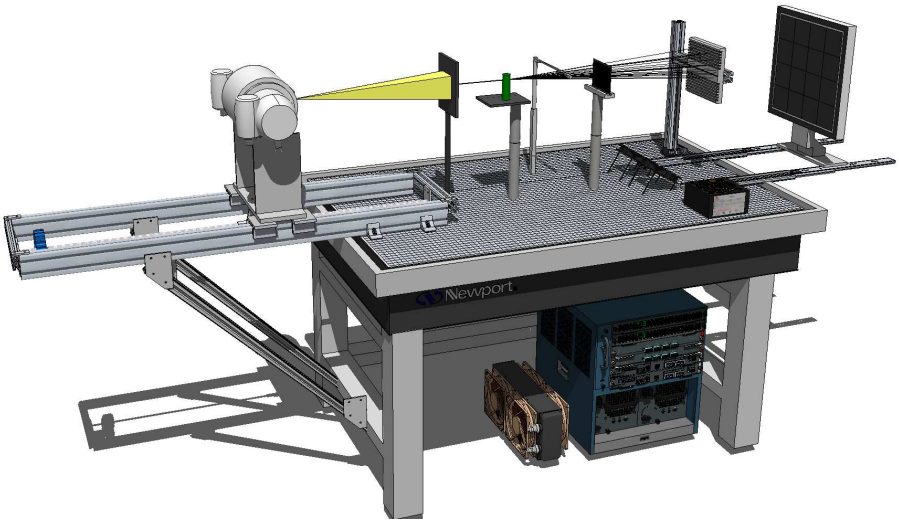

(c) Schematic

FIGURE 6.1: The experimental setup used in this work. Shown from left to right is the x-ray tube, pinhole collimator, the sample, the lead attenuator, the coded aperture mask, the photon counting detector, and the flat-panel energy integrating detector. In (a), the letters stand for 'S': scatter Shield, 'C': pinhole Collimator, 'M': coded aperture Mask, 'D': Detector. The coded aperture in (b) modulates the detected scattered X-rays to enable resolution along the beam direction, eliminating the need to rotate the sample as in tomography.

6.2.3 Tissue histology, radiography and image registration

In order to aid in the volumetric registration of the x-ray scatter imaging with the histology sections of the breast tissue sample, we acquired high resolution (21 line-pairs per mm) x-ray transmission radiographs of the sample. The transmission imaging was performed using the Faxitron BioVision^{+} surgical specimen radiography system comprising a 50 kV, 1 mA molybdenum source with 11 μm focal spot size and 0.254 mm beryllium filtration and a high-resolution detector providing 24 μmm spatial resolution.

After the breast issue specimen was imaged using radiography, it underwent routine clinical histological processing: it was dehydrated, cleared, infiltrated and embedded in paraffin wax, sectioned using a rotary microtome, and then stained using H&E staining [122]. The stained tissue slides were then interpreted by a pathologist who identified suspicious regions for the presence of cancer.

Because of the small thickness (5 mm) of the sample relative to its width (2.5 cm), the image registration for this specimen was straightforward in one of the three dimensions. Therefore, the image registration task for this specimen involved only the remaining two dimensions, and the interpreted tissue histology slides and the x-ray coherent scatter images could be registered based on the 2D high-resolution radiography image. We identified visible characteristic features of the boundary of the tissue sample in the radiographs, histological images (stained slides) and x-ray coherent scatter image and used them to align the three images in cross-section. It is assumed that minimal but evident feature distortions resultant from the histological processing will exist but should not be significant as to hinder the comparison of CACSSI with surgical pathology. The claim must also be made that the CACSSI image voxel depth is equal to the tumor thickness but the pathological slice analyzed was only 20-30 μm in thickness. We therefore chose to have the pathologist interpret

a slice taken from the center of the tumor (2.5 mm depth) such that partial volume averaging effects were minimized (because features and tissue composition are not necessarily uniform through the full 5 mm tumor thickness).

6.3 Results

Experimental coherent scatter images for the cancerous breast tissue sample are shown in Fig. 6.2(b)-(d), and volume renderings of the four types of breast tissue classified in the sample are shown in Fig. 6.3. Figure 6.2(b) shows the volume rendering of the sample based on its measured scatter intensity, and Fig. 6.2(c) shows the scatter intensity for a single slice through the sample. Figure 6.2(d) shows the material identification results for the sample with the material type in each pixel classified as one of the four available tissue types: Cancerous (black), normal (red), adipose (blue) tissue (Note: fibroglandular tissue was not explicitly detected in this slice). As expected for this cancerous tissue sample, the classified image showed several pixels of cancerous tissue, which are visible in Fig. 6.2(d) in the region labeled 'A'. It can be seen that the scatter intensity alone from Fig. 6.2(c), which would be akin to the transmission image, is insufficient to identify regions of cancer.

Figure 6.4(a) shows the coherent scatter differential cross sections reconstructed at pixel locations labeled 'A', 'B', and 'C' in Fig. 6.2(d). For reference, Fig. 6.4(b) shows the expected coherent scatter differential cross sections from Kidane et al for cancerous, normal and adipose tissue. The correlation of the curves in Fig. 6.4(a) to those in Fig. 6.4(b) is the basis used for classifying the type of tissue in the voxel. The normal and adipose curves measured experimentally in this study strongly resembled the average curves reported by Kidane et al, whereas the carcinoma curves measured here deviated to a certain degree from those reported by Kidane et al. These deviations in our sample could stem from structural changes caused by repeated thawing and freezing of the specimen.

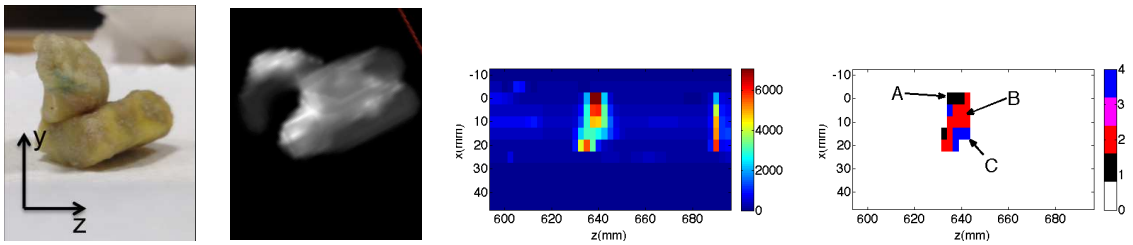

(a) (b) (c) (d)

FIGURE 6.2: Images of the cancerous breast tissue sample scanned experimentally. The scatter intensity reconstructed from the sample is visualized in (b) and (c), whereas the pixels classified into different tissue-types is shown in (d). In (d) white is air, black is cancerous tissue, red is normal tissue, magenta is fibroglandular tissue, and blue is adipose tissue. The results show that the coherent scatter imaging system is able to detect cancerous voxels inside of the breast tissue sample that was known ahead of time to be cancerous.

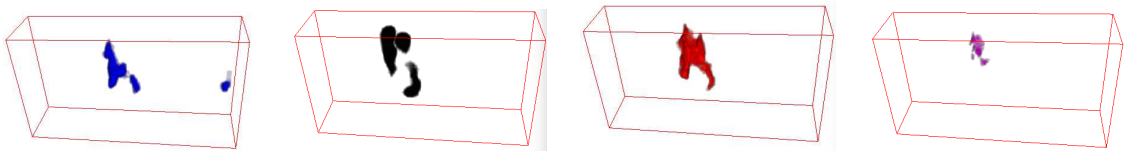

(a) Adipose (b) Cancerous (c) Normal (d) Fibroglandular

FIGURE 6.3: Volume renderings of the four types of tissue in the cancerous tissue sample based on voxel classification results of the reconstructed coherent scatter image from Fig. 6.2. The coherent scatter imaging technique can be used to determine the distribution of cancerous tissue through the volume, which would prove to be an important capability for diagnostic medical applications such as surgical margin detection.

Experimental images for the healthy breast tissue specimen from the same patient are shown in Fig. 6.5. The material-classified image in Fig. 6.5(c) shows that no cancerous tissue was present in the sample.

The classified image for the third sample (with each pixel identified as a specific type or mixture of breast tissues) is shown in Fig. 6.6(a). The colorbar represents the probability of malignancy in each voxel, determined through the location and intensities of momentum transfer peaks in the reconstructed spectra as well as overall form factor shape. This method was used to account for partial volume spectral averaging

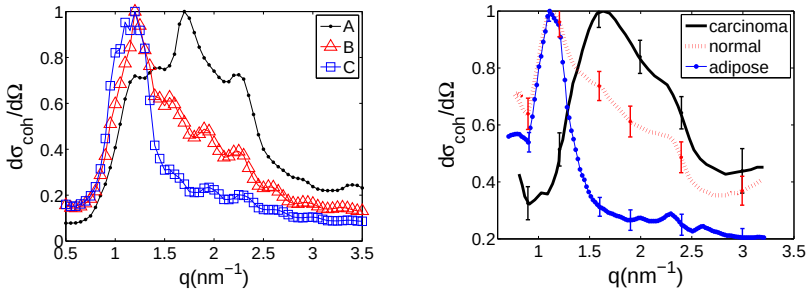

(a) Voxels from Fig. 6.2(d) (b) Literature

FIGURE 6.4: Comparison of the (a) coherent scatter differential cross sections reconstructed for the voxels labeled in Fig. 6.2(d) with (b) those from validated X-ray diffraction measurements of homogeneous samples from Kidane et al [1]. The correlation of the curves in (a) to those in (b) enables the tissue identification performed in this work.

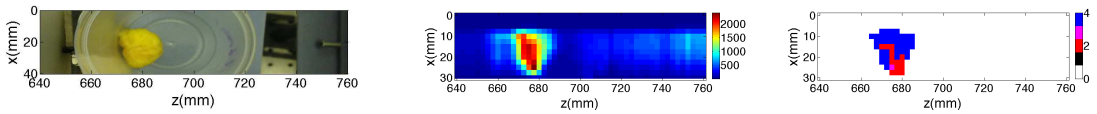

(a) Photograph (b) Scatter Intensity (c) Classification results

FIGURE 6.5: Images of the healthy breast tissue sample. As in Fig. 6.2(d), the color scheme used here in Fig. 6.5(c) is white (air), black (cancerous tissue), red (normal tissue), magenta (fibroglandular tissue), and blue (adipose tissue). The results show that the coherent scatter imaging system is able to rule out the presence of cancerous voxels in this breast tissue sample, which was known *a priori* to be healthy.

of sub-voxel sized features of differing tissues. In order to aid in the qualitative visual comparison with the histology results, shown in Fig. 6.6(c), we linearly interpolated the classification results onto a finer pixel grid to model the partial voluming effect for features smaller than the pencil beam width in Fig. 6.6(b). The radiography image used for aiding the image registration is shown in Fig. 6.6(d). We can see that there is overlap between the white pixels–indicating the highest probability for cancer presence in the CACSSI classification results–and the dark regions in the tissue histology–indicating the presence of cancer due to a high density of cells infiltrating and filling the intraluminal space of the ducts. This strong match demonstrates the

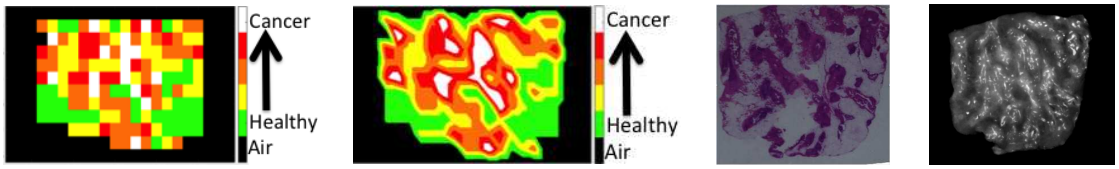

(a) CACSSI (b) interpolated (c) histology (d) radiograph

FIGURE 6.6: Results of the study, where (a) shows the classified CACSSI image, (b) the classified image after linear interpolation to have a smaller voxel size, (c) the tissue histology results, and (d) the radiography image. In (a) and (b), black represents air, green represents healthy tissue, and white represents cancerous tissue. The colors yellow, orange and red each represent tissue that has successively greater percentages of cancerous tissue in the voxel or that are more likely to be cancerous tissue. The excellent match between the white regions in (a) and (b)–representing voxels with reconstructed differential coherent scatter cross sections with a high degree of overlap with the known signal from cancer–and the dark stained regions in (d) demonstrates the accuracy of the CACSSI technique for cancer localization.

ability of CACSSI to potentially serve as a proxy for ex vivo histology.

6.4 Discussion

In this chapter, we first measured coherent scatter cross-sections and compared them against theoretical values reported in literature. The match between the experimental and theoretical differential coherent scatter cross sections not only demonstrates the utility of coherent scatter imaging in cancer detection, but also indicates the presence of population-invariant attributes that make X-ray diffraction useful for tissue identification and differentiation. The coherent scatter imaging system accurately determined the nature of the specimen (i.e., malignant or healthy) by identifying the tissue type in each voxel within the specimen. Cancer was found only in the specimen known to be malignant, whereas the specimen known to be healthy was classified as normal.

In addition, we validated the spatial accuracy of CACSSI for cancer localization by comparing the CACSSI scatter image with histological analysis. The demon-

strated accuracy of CACSSI for cancer identification opens the door for applications requiring non-invasive radiation biopsy; for example in vivo breast tumor identification and ex vivo surgical margin detection in breast lumpectomy procedures, where the clinical task is to rule out the presence of cancer at the boundary of the surgical specimen.

There are some discrepancies between the CACSSI results and the histology that are caused by artifacts from (a) the shrinkage that occurs during the dehydration step of the histology pre-processing; and (b) the presence of water in the sample due to repeated thawing and freezing of the sample as it has been used in imaging experiments over several years. Future work will focus on using fresh tissue samples obtained directly from mastectomy and lumpectomy patients at the histological preparatory stage to prevent any potential artifacts from freezing and staining.

6.5 Conclusion

We showed in this work that coded aperture coherent scatter spectral imaging is able to classify the spatial distribution of cancer inside an ex vivo breast sample with high accuracy as validated by histology. This accuracy of CACSSI shows that it is a potential proxy for tissue histology. Unlike tissue histology, CACSSI images of surgically excised tissue samples can be acquired in real-time with minimal processing compared to current histology specimen prep techniques. Future steps will focus on acquiring experimental results on a population of fresh tissue samples obtained through surgical resections.

7

Conclusions & future work

7.1 Conclusions

The aim of this work is to develop coherent scatter imaging for intra-operative margin detection during breast conserving surgery (BCS) (a.k.a. lumpectomy) procedures to achieve improved accuracy and speed over currently available methods in clinical practice. We accomplished this goal by exploring two coherent scatter imaging techniques using Monte Carlo (MC) simulations, determining the advantages and disadvantages of each, and then implementing the most practical and realistic coherent scatter imaging system in experiment. The initial development of the two imaging systems focused on identifying the most suitable imaging parameters such as X-ray energy, detectors, and coded-aperture mask designs. Then we determined each system's efficacy based on its accuracy for classifying individual voxels within heterogeneous breast tissue specimens as being cancerous or healthy. Finally, as is done for any new medical technology, we performed a virtual clinical trial to demonstrate the efficacy of the two new technologies in intra-operative margin detection during BCS procedures. Our experimental implementation of the coherent scatter

imaging method was validated against tissue histology of the breast cancer specimen that was imaged.

In Chapter 1, we presented an introduction to breast conserving surgery, margin detection, and coherent scatter imaging, and we described the principle of our proposed method. In Chapter 2, we developed and validated our MC simulation for modeling coherent scatter against experiment. The results showed a strong match with experiment, demonstrating the validity of the MC simulation for the system optimization processes in Chapters 3, 4, and 5.

In Chapter 3, we then designed a coherent scatter computed tomography (CSCT) system for breast cancer imaging. Using simulations, we demonstrated that the CSCT system could automatically detect cancerous voxels in the resected tissue specimen with high accuracy and spatial resolution. Using ROC analysis, we demonstrated an AUC of 0.97 for the task of cancerous voxel detection inside a simulated BCS specimen.

Using the same study design and evaluative analysis as we did for CSCT, in Chapter 4 we designed and optimized a coded aperture coherent scatter spectral imaging (CACSSI) system. The AUC for this system for cancerous voxel classification was found to be 0.94. In addition, this method was at least one order of magnitude faster than CSCT (CSCT would require on the order of 30 minutes for a three-dimensional scan of a BCS specimen, whereas CACSSI would require on the order of 3 minutes).

In Chapter 5, we used virtual clinical trials to show that CSCT and CACSSI could accurately perform the task of intra-operative margin detection with AUC values of 0.975 and 0.741, respectively.

Finally, in Chapter 6, we implemented a real optimized CACSSI system and demonstrated its ability to accurately classify cancerous breast tissue by confirming against tissue histology.

The results of this work, i.e., the AUC values for CSCT and CACSSI for the tasks

of cancerous voxel detection and intra-operative margin detection (i.e., the virtual clinical trials), and the experimental validation of CACSSI against tissue histology demonstrate that coherent scatter imaging has strong potential to provide quick and accurate imaging of tumors for intra-operative margin assessment. Unlike tissue histology, both CSCT and CACSSI can be performed intra-operatively (i.e., within minutes of the surgery while the surgeon and patient are still in the operating room).

The coherent scatter imaging method therefore has the potential to address the following needs for intra-operative techniques.

1. Coherent scatter imaging can potentially provide a more accurate overall assessment of the specimen by imaging the tumor in its entirety.

2. It can automatically classify the spatial distribution of cancer through bimolecular properties of the tumor.

3. It can do so intra-operatively and within minutes of surgery while the patient is still under anesthesia.

4. Coherent scatter images can be automatically analyzed to identify tumor margins and provide a binary positive/negative result.

In contrast, FSA, touch-prep and tissue histology, all require substantial amounts of manual human resources such as trained pathology technicians and pathologists.

When comparing CSCT and CACSSI to each other, we found that CSCT outperformed CACSSI in accuracy (by $\sim$5% for cancerous voxel detection and $\sim$24% for intra-operative margin detection). The much larger discrepancy in performance between the two imaging techniques for intra-operative margin detection could be due to spatial resolution (the main technical measure of imaging performance where CSCT outperforms CACSSI) being much more important for the task of margin detection than for classifying individual voxels. For margin detection, the ability

to accurately detect a single point where a tumor makes contact with a specimen boundary is highly dependent on the imaging system's ability to image with fine resolution. Whereas the ability to classify a given voxel within the field of view may in fact actually worsen with improved spatial resolution since smaller voxels provide less signal.

However, CSCT requires significantly longer scan times (on the order of 3 minutes for CACSSI versus 30 minutes for CSCT). The scan time represents actual wait time for the clinical team (with the patient under anesthesia), and therefore it is an important factor to be taken into consideration.

We believe that CSCT outperformed CACSSI primarily due to the differences in spatial resolution between the two techniques. Although CACSSI spatial resolution can be improved using a higher spatial frequency coded aperture mask, it leads to lesser signal from each voxel, making the system more susceptible to noise. In our system, using higher spatial frequency masks degraded the performance primarily due to the higher noise in the system. There is potential to improve the clinical efficacy of CACSSI by reducing the noise in the system as well as improving the noise modeling in the reconstruction algorithm (which is discussed in the next subsection).

With improvements in the reconstruction algorithm, CACSSI could potentially match CSCT in clinical accuracy and while enjoying the advantage of shorter scan time. It has strong potential to be used in the operating room during BCS procedures, providing full 3D images of the BCS specimen with the cancerous voxels automatically classified. Such technology would assist clinicians in more accurately assessing tumor margins in surgery. The improved accuracy of the technology over currently used clinical techniques could reduce the rate of repeat BCS surgeries and reduce the cost of the initial BCS procedures by eliminating the need to wait the 17-20 minutes and to employ trained pathology personnel required for FSA or touch-prep cytology.

7.2 Future work

A majority (Chapters 3, 4, and 5) of the development of CSCT and CACSSI for cancer imaging and for intra-operative margin detection in this dissertation was performed using Monte Carlo simulations. Because experiments and physical implementations of the imaging systems do not allow for as precise control of the imaging system setup–such as precise angular and spatial alignments of various components–and because experimental imaging systems have additional background noise, an important next step of this work to further bolster its potential clinical value is to qualitatively and quantitatively evaluate its accuracy for cancer imaging and intra-operative margin detection in an experimental or real-world scenario. The experimental validation of the CACSSI imaging results with tissue histology that was carried out in this dissertation (Chapter 6) was done qualitatively and only for a single specimen. In order to formally validate CACSSI, an important next step is to quantitatively evaluate the correlation of the CACSSI images with tissue histology, and to do so for a population of samples.

The most important future step for CACSSI is to improve its resolution by optimizing coded-aperture masks and modifying the reconstruction algorithm to better model noise in the system. This approach will allow more robust reconstruction of the signal from high frequency coded aperture masks, thereby bringing the resolution of the CACSSI system closer to that of CSCT. Investigating the application of regularization and smoothing algorithms such as total variation (TV) [123] may allow us to improve these reconstructions of extended objects when using higher frequency masks in order to improve the overall performance of CACSSI for breast cancer detection.

Alternatively, one could reduce the scan time required for CSCT to make it more suitable for intra-operative clinical use. This goal could be achieved using the

same strategies that are currently used for scan-time reduction and dose reduction in conventional x-ray CT; for example implementing fan-beam geometries, iterative or model-based reconstruction, and compressive sensing techniques [124, 125].

Instead of focusing on improving the resolution of CACSSI or reducing the scan time of CSCT, we could develop an imaging approach that is a hybrid of CACSSI and CSCT, i.e., acquiring CACSSI data at a second, and potentially even a third, angular perspective and using that additional data to improve the reconstructed image resolution and signal. Such a hybrid approach would allow us to exploit the accuracy we demonstrated for CSCT in this work and the reduced scan time of CACSSI.

Another strategy to improve the spatial resolution for CACSSI is to use coded aperture masks that have unique patterns in two dimensions, instead of only having a pattern along one dimension as in this work. A 2D coded aperture mask would allow us to more precisely modulate the scatter signal and therefore better resolve the sample. The biggest challenge with implementing 2D coded apertures is acquiring a 2D photon counting detector to measure the modulations in both dimensions.

In addition, for successful translation to the clinic, we must also expand the experimental work described in Chapter 6 through future clinical or pre-clinical trials.

Bibliography

[1] G. Kidane, R. D. Speller, G. J. Royle, and a. M. Hanby, "X-ray scatter signatures for normal and neoplastic breast tissues." *Phys Med Biol*, vol. 44, no. 7, pp. 1791–802, jul 1999.

[2] D. M. Cunha, O. R. Oliveira, C. A. Pérez, and M. E. Poletti, "X-ray scattering profiles of some normal and malignant human breast tissues," *X Ray Spectrom*, vol. 35, no. 6, pp. 370–374, nov 2006.

[3] E. a. Ryan and M. J. Farquharson, "Breast tissue classification using x-ray scattering measurements and multivariate data analysis," *Phys Med Biol*, vol. 52, no. 22, pp. 6679–6696, nov 2007.

[4] A. L. C. Conceição, M. Antoniassi, and M. E. Poletti, "Analysis of breast cancer by small angle X-ray scattering (SAXS)." *Analyst*, vol. 134, no. 6, pp. 1077–82, jun 2009.

[5] W. M. Elshemey, O. S. Desouky, M. M. Fekry, S. M. Talaat, and A. a. Elsayed, "The diagnostic capability of x-ray scattering parameters for the characterization of breast cancer," *Med Phys*, vol. 37, no. 8, p. 4257, 2010.

[6] S. Pani, E. J. Cook, J. a. Horrocks, J. L. Jones, and R. D. Speller, "Characterization of breast tissue using energy-dispersive X-ray diffraction computed tomography." *Appl Radiat Isot*, vol. 68, no. 10, pp. 1980–7, oct 2010.

[7] S. Sidhu, G. Falzon, S. a. Hart, J. G. Fox, R. a. Lewis, and K. K. W. Siu, "Classification of breast tissue using a laboratory system for small-angle x-ray scattering (SAXS)." *Phys Med Biol*, vol. 56, no. 21, pp. 6779–91, nov 2011.

[8] W. M. Elshemey, F. S. Mohamed, and I. M. Khater, "X-ray scattering for the characterization of lyophilized breast tissue samples," *Radiat Phys Chem*, vol. 90, pp. 67–72, sep 2013.

[9] W. P. Segars, A. I. Veress, J. R. Wells, G. M. Sturgeon, N. Kiarashi, J. Y. Lo, E. Samei, and J. T. Dobbins, "Population of 100 realistic, patient-based

computerized breast phantoms for multi-modality imaging research," in *SPIE Medical Imaging*. International Society for Optics and Photonics, 2014, pp. 90 331X–90 331X.

[10] J. Solomon, R. Nelson, and E. Samei, "Tu-c-103-01: A framework for 3d modeling of anthropomorphic lesions in ct," *Medical Physics*, vol. 40, no. 6, pp. 436–436, 2013.

[11] M. N. Lakshmanan, B. P. Harrawood, E. Samei, and A. J. Kapadia, "Volumetric x-ray coherent scatter imaging of cancer in resected breast tissue: a Monte Carlo study using virtual anthropomorphic phantoms," *Physics in Medicine and Biology*, vol. 60, no. 16, pp. 6355–6370, 2015.

[12] M. N. Lakshmanan, A. J. Kapadia, P. Sahbaee, S. D. Wolter, B. P. Harrawood, D. Brady, and E. Samei, "An X-ray scatter system for material identification in cluttered objects: A Monte Carlo simulation study," *Nucl. Instr. Meth. Phys. Res. B*, vol. 335, pp. 31–38, sep 2014.

[13] American Cancer Society. (2013, Aug) Breast cancer.

[14] C. E. DeSantis, C. C. Lin, A. B. Mariotto, R. L. Siegel, K. D. Stein, J. L. Kramer, R. Alteri, A. S. Robbins, and A. Jemal, "Cancer treatment and survivorship statistics, 2014," *CA: a cancer journal for clinicians*, vol. 64, no. 4, pp. 252–271, 2014.

[15] E. S. Hwang, D. Y. Lichtensztajn, S. L. Gomez, B. Fowble, and C. A. Clarke, "Survival after lumpectomy and mastectomy for early stage invasive breast cancer," *Cancer*, vol. 119, no. 7, pp. 1402–1411, 2013.

[16] J. C. Cendán, D. Coco, and E. M. Copeland, "Accuracy of intraoperative frozen-section analysis of breast cancer lumpectomy-bed margins." *J Am Coll Surgeons*, vol. 201, no. 2, pp. 194–8, aug 2005.

[17] M. D. Keller, S. K. Majumder, M. C. Kelley, I. M. Meszoely, F. I. Boulos, G. M. Olivares, and A. Mahadevan-Jansen, "Autofluorescence and diffuse reflectance spectroscopy and spectral imaging for breast surgical margin analysis." *Laser Surg Med*, vol. 42, no. 1, pp. 15–23, jan 2010.

[18] L. Jacobs, "Positive margins: the challenge continues for breast surgeons." *Ann Surg Oncol*, vol. 15, no. 5, pp. 1271–2, may 2008.

[19] M. S. Moran, "Should low-risk patients be treated with three-dimensional conformal radiation therapy-accelerated partial-breast irradiation in an

off-protocol setting?" *Journal of clinical oncology : official journal of the American Society of Clinical Oncology*, vol. 31, no. 32, pp. 4032–7, nov 2013. [Online]. Available: http://www.ncbi.nlm.nih.gov/pubmed/24081936

[20] T. A. King, R. Sakr, S. Patil, I. Gurevich, M. Stempel, M. Sampson, and M. Morrow, "Clinical management factors contribute to the decision for contralateral prophylactic mastectomy," *Journal of Clinical Oncology*, vol. 29, no. 16, pp. 2158–2164, 2011.

[21] T. M. Bydlon, S. A. Kennedy, L. M. Richards, J. Q. Brown, B. Yu, M. K. Junker, J. Gallagher, J. Geradts, L. G. Wilke, and N. Ramanujam, "Performance metrics of an optical spectral imaging system for intra-operative assessment of breast tumor margins," *Optics Express*, vol. 18, no. 8, pp. 8058–8076, 2010.

[22] G. C. Balch, S. K. Mithani, J. F. Simpson, and M. C. Kelley, "Accuracy of intraoperative gross examination of surgical margin status in women undergoing partial mastectomy for breast malignancy," *The American surgeon*, vol. 71, no. 1, pp. 22–28, 2005.

[23] E. K. Valdes, S. K. Boolbol, J.-M. Cohen, and S. M. Feldman, "Intra-operative touch preparation cytology; does it have a role in re-excision lumpectomy?" *Annals of surgical oncology*, vol. 14, no. 3, pp. 1045–50, mar 2007.

[24] A. M. Laughney, V. Krishnaswamy, E. J. Rizzo, M. C. Schwab, R. J. Barth, B. W. Pogue, K. D. Paulsen, and W. a. Wells, "Scatter spectroscopic imaging distinguishes between breast pathologies in tissues relevant to surgical margin assessment." *Clinical cancer research : an official journal of the American Association for Cancer Research*, vol. 18, no. 22, pp. 6315–25, nov 2012.

[25] D. Carter, "Margins of lumpectomy for breast cancer," *Human pathology*, vol. 17, no. 4, pp. 330–332, 1986.

[26] F. D'Halluin, P. Tas, S. Rouquette, C. Bendavid, F. Foucher, H. Meshba, J. Blanchot, O. Coué, and J. Levêque, "Intra-operative touch preparation cytology following lumpectomy for breast cancer: a series of 400 procedures," *The Breast*, vol. 18, no. 4, pp. 248–253, 2009.

[27] J. S. Suri and R. M. Rangayyan, *Recent advances in breast imaging, mammography, and computer-aided diagnosis of breast cancer*. SPIE press, 2006, vol. 155.

[28] I. Pappo, R. Spector, A. Schindel, S. Morgenstern, J. Sandbank, L. T. Leider, S. Schneebaum, S. Lelcuk, and T. Karni, "Diagnostic performance of a novel device for real-time margin assessment in lumpectomy specimens," *Journal of Surgical Research*, vol. 160, no. 2, pp. 277–281, 2010.

[29] S. Kennedy, J. Geradts, T. Bydlon, J. Q. Brown, J. Gallagher, M. Junker, W. Barry, N. Ramanujam, and L. Wilke, "Optical breast cancer margin assessment: an observational study of the effects of tissue heterogeneity on optical contrast." *Breast cancer research : BCR*, vol. 12, no. 6, p. R91, jan 2010.

[30] M. D. Keller, E. Vargis, N. de Matos Granja, R. H. Wilson, M.-A. Mycek, M. C. Kelley, and A. Mahadevan-Jansen, "Development of a spatially offset Raman spectroscopy probe for breast tumor surgical margin evaluation." *Journal of biomedical optics*, vol. 16, no. 7, p. 077006, jul 2011.

[31] I. J. Bigio, "Real-time pathology to guide breast surgery: seeing alone is not believing." *Clinical cancer research : an official journal of the American Association for Cancer Research*, vol. 18, no. 22, pp. 6083–5, nov 2012.

[32] A. Momose, T. Takeda, Y. Itai, and K. Hirano, "Phase-contrast x-ray computed tomography for observing biological soft tissues." *Nature medicine*, no. 2, pp. 473–5, 1996.

[33] F. Pfeiffer, T. Weitkamp, O. Bunk, and C. David, "Phase retrieval and differential phase-contrast imaging with low-brilliance x-ray sources," *Nature physics*, vol. 2, no. 4, pp. 258–261, 2006.

[34] F. Zhang, G. Long, L. Levine, J. Ilavsky, and P. Jemian, "Quantitative characterization of the contrast mechanisms of ultra-small-angle x-ray scattering imaging," *Journal of Applied Crystallography*, vol. 41, no. 2, pp. 416–427, 2008.

[35] J. a. Greenberg, M. Hassan, K. Krishnamurthy, and D. Brady, "Structured illumination for tomographic X-ray diffraction imaging." *The Analyst*, vol. 139, no. 4, pp. 709–13, feb 2014.

[36] W. Friedrich, P. Knipping, and M. v. Laue, "Interference appearances in x-rays," *Ann. Phys.(Berlin)*, vol. 41, pp. 971–988, 1913.

[37] W. Bragg and W. Bragg, "The reflection of x-rays by crystals," *Proceedings of the Royal Society of London. Series A*, vol. 88, no. 605, pp. 428–438, 1913.

[38] J. D. Watson, F. H. Crick *et al.*, "Molecular structure of nucleic acids," *Nature*, vol. 171, no. 4356, pp. 737–738, 1953.

[39] P. Debye and P. Scherrer, "Interferenzen an regellos orientierten teilchen im röntgenlicht. i." *Nachrichten von der Gesellschaft der Wissenschaften zu Göttingen, Mathematisch-Physikalische Klasse*, vol. 1916, pp. 1–15, 1916.

[40] A. W. Hull, "A new method of x-ray crystal analysis," *Physical Review*, vol. 10, no. 6, p. 661, 1917.

[41] P. C. Johns, R. J. Leclair, and M. P. Wismayer, "Medical x-ray imaging with scattered photons," in *Opto-Canada: SPIE Regional Meeting in Optoelectronics, Photonics and Imaging, SPIE TD*, vol. 1, 2002, pp. 355–357.

[42] O. S. Desouky, W. M. Elshemey, and N. S. Selim, "X-ray scattering signatures of β-thalassemia," *Nuclear Instruments and Methods in Physics Research Section A: Accelerators, Spectrometers, Detectors and Associated Equipment*, vol. 607, no. 2, pp. 463–469, 2009.

[43] W. M. Elshemey, F. S. Abdelhady, and I. M. Khater, "X-ray scattering for the characterization of lyophilized breast tissue samples," *Radiation Physics and Chemistry*, 2013.

[44] G. Harding and B. Schreiber, "Coherent x-ray scatter imaging and its applications in biomedical science and industry," *Radiation physics and chemistry*, vol. 56, no. 1, pp. 229–245, 1999.

[45] R. W. Madden, J. Mahdavieh, R. C. Smith, and R. Subramanian, "An explosives detection system for airline security using coherent x-ray scattering technology," in *Optical Engineering+ Applications*. International Society for Optics and Photonics, 2008, pp. 707 915–707 915.

[46] G. Harding, "X-ray scatter tomography for explosives detection," *Radiation Physics and Chemistry*, vol. 71, no. 3-4, pp. 869–881, oct 2004.

[47] C. R. F. Castro, R. C. Barroso, and R. T. Lopes, "Scattering signatures for some human tissues using synchrotron radiation," *X Ray Spectrom*, vol. 34, no. 6, pp. 477–480, nov 2005.

[48] A. L. C. Conceição, M. Antoniassi, W. Geraldelli, and M. E. Poletti, "Mapping transitions between healthy and pathological lesions in human breast tissues by diffraction enhanced imaging computed tomography (DEI-CT) and small angle x-ray scattering (SAXS)," *Radiation Physics and Chemistry*, feb 2013.

[49] D. L. Batchelar, M. T. M. Davidson, W. Dabrowski, and I. a. Cunningham, "Bone-composition imaging using coherent-scatter computed tomography: Assessing bone health beyond bone mineral density," *Medical Physics*, vol. 33, no. 4, p. 904, 2006.

[50] M. Poletti, O. Goncalves, and I. Mazzaro, "X-ray scattering from human breast tissues and breast-equivalent materials," *Phys Med Biol*, vol. 47, no. 1, p. 47, 2002.

[51] E. Ryan and M. Farquharson, "Angular dispersive x-ray scattering from breast tissue using synchrotron radiation," *Radiat Phys Chem*, vol. 71, no. 3, pp. 971–972, 2004.

[52] R. a. Lewis, K. D. Rogers, C. J. Hall, E. Towns-Andrews, S. Slawson, A. Evans, S. E. Pinder, I. O. Ellis, C. R. Boggis, a. P. Hufton, and D. R. Dance, "Breast cancer diagnosis using scattered X-rays." *Proc SPIE*, vol. 4320, pp. 547–554, sep 2001.

[53] C. Theodorakou and M. J. Farquharson, "Human soft tissue analysis using x-ray or gamma-ray techniques." *Phys Med Biol*, vol. 53, no. 11, pp. R111–49, jun 2008.

[54] K. Gelse, E. Pöschl, and T. Aigner, "Collagens?structure, function, and biosynthesis," *Advanced drug delivery reviews*, vol. 55, no. 12, pp. 1531–1546, 2003.

[55] S. Kauppila, F. Stenbäck, J. Risteli, A. Jukkola, and L. Risteli, "Aberrant type i and type iii collagen gene expression in human breast cancer in vivo," *The Journal of pathology*, vol. 186, no. 3, pp. 262–268, 1998.

[56] G. Harding, J. Kosanetzky, and U. Neitzel, "X-ray diffraction computed tomography," *Medical physics*, vol. 14, p. 515, 1987.

[57] J.-P. Schlomka, A. Harding, U. Van Stevendaal, M. Grass, and G. L. Harding, "Coherent scatter computed tomography: a novel medical imaging technique," in *Medical Imaging 2003*. International Society for Optics and Photonics, 2003, pp. 256–265.

[58] K. MacCabe, K. Krishnamurthy, A. Chawla, D. Marks, E. Samei, and D. Brady, "Pencil beam coded aperture x-ray scatter imaging," *Optics Express*, vol. 20, no. 15, pp. 16 310–16 320, 2012.

[59] D. L. Batchelar and I. A. Cunningham, "Material-specific analysis using coherent-scatter imaging," *Medical Physics*, vol. 29, no. 8, p. 1651, 2002.

[60] G. Harding, J. Kosanetzky, and U. Neitzel, "Elastic scatter computed tomography." *Physics in medicine and biology*, vol. 30, no. 2, pp. 183–6, mar 1985.

[61] B. Ghammraoui and A. Badal, "Monte Carlo simulation of novel breast imaging modalities based on coherent x-ray scattering." *Physics in medicine and biology*, vol. 59, no. 13, pp. 3501–16, jul 2014.

[62] J. Griffiths, G. Royle, J. Horrocks, A. Hanby, S. Pani, and R. Speller, "Angular dispersive diffraction microCT of small breast tissue samples," *Radiation Physics and Chemistry*, vol. 77, no. 4, pp. 373–380, apr 2008.

[63] J.-P. Schlomka, A. Harding, U. van Stevendaal, M. Grass, and G. L. Harding, "Coherent Scatter Computed Tomography - A Novel Medical Imaging Technique," *Proc. of SPIE*, vol. 5030, pp. 256–265, jun 2003.

[64] K. G. Lewis, "Coherent Scatter Computed Tomography (CSCT) - A Monte Carlos Simulation Study," Ph.D. dissertation, Vanderbilt University, 2013.

[65] M. S. Westmore, A. Fenster, and I. a. Cunningham, "Tomographic imaging of the angular-dependent coherent-scatter cross section." *Medical physics*, vol. 24, no. 1, pp. 3–10, jan 1997.

[66] M. T. M. Davidson, D. L. Batchelar, S. Velupillai, J. D. Denstedt, and I. a. Cunningham, "Laboratory coherent-scatter analysis of intact urinary stones with crystalline composition: a tomographic approach." *Physics in medicine and biology*, vol. 50, no. 16, pp. 3907–25, aug 2005.

[67] U. van Stevendaal, J.-P. Schlomka, A. Harding, and M. Grass, "A reconstruction algorithm for coherent scatter computed tomography based on filtered back-projection," *Medical Physics*, vol. 30, no. 9, p. 2465, 2003.

[68] G. Harding, M. Newton, and J. Kosanetzky, "Energy-dispersive X-ray diffraction tomography," *Physics in Medicine and Biology*, vol. 35, no. 1, pp. 33–41, jan 1990.

[69] A. Dicken, K. Rogers, P. Evans, J. W. Chan, J. Rogers, and S. Godber, "Combined X-ray diffraction and kinetic depth effect imaging." *Optics express*, vol. 19, no. 7, pp. 6406–13, mar 2011. [Online]. Available: http://www.ncbi.nlm.nih.gov/pubmed/21451668

[70] K. MacCabe, K. Krishnamurthy, A. Chawla, D. Marks, E. Samei, and D. Brady, "Pencil beam coded aperture x-ray scatter imaging," *Optics Express*, vol. 20, no. 15, p. 16310, jul 2012.

[71] J. A. Greenberg, K. Krishnamurthy, and D. Brady, "Snapshot molecular imaging using coded energy-sensitive detection," *Optics Express*, vol. 21, no. 21, 2013.

[72] S. Agostinelli, J. Allison, K. Amako, J. Apostolakis, H. Araujo, P. Arce *et al.*, "Geant4—a simulation toolkit," *Nucl Instrum Meth A*, vol. 506, no. 3, pp. 250–303, 2003.

[73] J. Allison, K. Amako, J. Apostolakis, H. Araujo, P. A. Dubois, M. Asai *et al.*, "Geant4 developments and applications," *IEEE Trans Nucl Sci*, vol. 53, no. 1, pp. 270–278, 2006.

[74] M. Batic, G. Hoff, M. G. Pia, and P. Saracco, "Photon elastic scattering simulation: validation and improvements to geant4," *IEEE Trans Nucl Sci*, vol. 59, no. 4, pp. 1636–1664, 2012.

[75] J. Baro, J. Sempau, J. Fernandez-Varea, and F. Salvat, "Penelope: an algorithm for monte carlo simulation of the penetration and energy loss of electrons and positrons in matter," *Nucl. Instr. Meth. Phys. Res. Sec. B*, vol. 100, no. 1, pp. 31–46, 1995.

[76] J. S. Hendricks, G. W. McKinney, L. S. Waters, T. L. Roberts, H. W. Egdorf, J. P. Finch, H. R. Trellue, E. J. Pitcher, D. R. Mayo, M. T. Swinhoe *et al.*, "Mcnpx extensions version 2.5. 0," *Los Alamos, NM: LANL Rep. LA-UR-04*, vol. 570, 2004.

[77] J. Briesmeister and L. A. N. Laboratory, *MCNP–A general Monte Carlo code for neutron and photon transport*. Los Alamos National Laboratory, 1986.

[78] M. N. Lakshmanan and A. J. Kapadia, "Quantitative assessment of lesion detection accuracy, resolution, and reconstruction algorithms in neutron stimulated emission computed tomography." *IEEE Trans. Med. Imag.*, vol. 31, no. 7, pp. 1426–35, jul 2012.

[79] M. N. Lakshmanan, B. P. Harrawood, G. a. Agasthya, and A. J. Kapadia, "Simulations of breast cancer imaging using gamma-ray stimulated emission computed tomography." *IEEE Trans. Med. Imag.*, vol. 33, no. 2, pp. 546–55, feb 2014.

[80] M. N. Lakshmanan, B. P. Harrawood, G. A. Agasthya, S. Member, G. Rusev, and A. J. Kapadia, "Nuclear Resonance Fluorescence (NRF) In GEANT4 : Development , Validation , and Testing," in *IEEE Nucl. Sci. Symp. & Med. Imag. Conference*, 2012, pp. 1731–1734.

[81] M. N. Lakshmanan, B. P. Harrawood, G. Rusev, G. a. Agasthya, and A. J. Kapadia, "Simulations of nuclear resonance fluorescence in Geant4," *Nucl. Instr. Meth. Phys. Res. A*, vol. 763, pp. 89–96, nov 2014.

[82] C. J. Leliveld, J. G. Maas, V. R. Bom, and C. W. E. van Eijk, "Monte Carlo modeling of coherent scattering: influence of interference," *IEEE Transactions on Nuclear Science*, vol. 43, no. 6, pp. 3315–3321, 1996.

[83] I. Kawrakow and D. Rogers, "O (2006) the egsnrc code system: Monte carlo simulation of electron and photon transport," *NRCC Report PIRS-701*.

[84] P. Johns and M. Yaffe, "Coherent scatter in diagnostic radiology," *Medical physics*, vol. 10, p. 40, 1983.

[85] J. Persliden and G. A. Carlsson, "Scatter rejection by air gaps in diagnostic radiology. calculations using a monte carlo collision density method and consideration of molecular interference in coherent scattering," *Physics in medicine and biology*, vol. 42, no. 1, p. 155, 1997.

[86] S. Cardoso, O. Goncalves, H. Schechter, and J. Eichler, "Modelling the elastic scattering in diagnostic radiology: the importance of structure form factors," *Physics in Medicine and Biology*, vol. 48, no. 13, p. 1907, 2003.

[87] G. Poludniowski, P. Evans, and S. Webb, "Rayleigh scatter in kilovoltage x-ray imaging: is the independent atom approximation good enough?" *Physics in Medicine and Biology*, vol. 54, no. 22, p. 6931, 2009.

[88] D. Cunha, A. Tomal, and M. Poletti, "Diffraction enhanced breast imaging through Monte Carlo simulations," *Nuclear Instruments and Methods in Physics Research Section A: Accelerators, Spectrometers, Detectors and Associated Equipment*, vol. 652, no. 1, pp. 878–882, oct 2011.

[89] W. M. Elshemey and W. B. Elsharkawy, "Monte Carlo simulation of x-ray scattering for quantitative characterization of breast cancer." *Physics in medicine and biology*, vol. 54, no. 12, pp. 3773–84, jun 2009.

[90] L. Hassan, L. Peerzada, K. Kern, and C. a. MacDonald, "Coherent scatter imaging simulation for screening mammography," *Proc. of SPIE*, vol. 8509, pp. 85 090C–85 090C–9, oct 2012.

[91] D. E. Cullen, J. H. Hubbell, and L. Kissel, "Epdl97: The evaluated photon data library,97 version," *UCRL-50400*, vol. 6, p. 1997, 1997.

[92] J. H. Hubbell, W. J. Viegele, E. A. Briggs, R. T. Brown, D. T. Cromer, and R. J. Hubbell, "Atomic form factors, incoherent scattering functions, and photon scattering cross sections," *J. Phys. Chem. Ref. Data*, vol. 4, pp. 471–538, 1975.

[93] E. Storm, "Calculated bremsstrahlung spectra from thick tungsten targets," *Physical Review A*, vol. 5, no. 6, p. 2328, 1972.

[94] ——, "Emission of characteristic l and k radiation from thick tungsten targets," *Journal of Applied Physics*, vol. 43, no. 6, pp. 2790–2796, 1972.

[95] E. Samei and M. J. Flynn, "An experimental comparison of detector performance for direct and indirect digital radiography systems," *Medical physics*, vol. 30, p. 608, 2003.

[96] A. Makeev, M. Rodriguez, G.-C. Wang, and S. J. Glick, "Modeling czt/cdte x-ray photon-counting detectors," in *SPIE Medical Imaging*. International Society for Optics and Photonics, 2015, pp. 94 124V–94 124V.

[97] M. N. Lakshmanan, A. J. Kapadia, B. P. Harrawood, D. Brady, and E. Samei, "X-ray coherent scatter imaging for surgical margin detection: a Monte Carlo study," in *Proc. of SPIE*, B. R. Whiting and C. Hoeschen, Eds., vol. 9033, mar 2014, p. 903361.

[98] G. Harding, J. Kosanetzky, and U. Neitzel, "X-ray diffraction computed tomography," *Med Phys*, vol. 14, no. 4, pp. 515–525, 1987.

[99] B. P. Harrawood, G. a. Agasthya, M. N. Lakshmanan, G. Raterman, and A. J. Kapadia, "Geant4 distributed computing for compact clusters," *Nucl. Instr. Meth. Phys. Res. A*, vol. 764, pp. 11–17, nov 2014.

[100] J. M. Boone, T. R. Fewell, and R. J. Jennings, "Molybdenum, rhodium, and tungsten anode spectral models using interpolating polynomials with application to mammography," *Med Phys*, vol. 24, p. 1863, 1997.

[101] J. Wells, P. Segars, and J. Dobbins, "Th-a-103-10: Improved segmentation of low-contrast fibroglandular structures in high-noise breast ct volumes for xcat modeling," *Medical Physics*, vol. 40, no. 6, pp. 527–527, 2013.

[102] J. Solomon and E. Samei, "A generic framework to simulate realistic lung, liver and renal pathologies in ct imaging," *Physics in medicine and biology*, vol. 59, no. 21, p. 6637, 2014.

[103] K. H. Ng, D. A. Bradley, and L. M. Looi, "Elevated trace element concentrations in malignant breast tissues," *Brit J Radiol*, vol. 70, pp. 375–382, 1997.

[104] G. Ullman, M. Sandborg, R. Hut, D. Dance, and G. Alm Carlsson, "Implementation of pathologies in the monte carlo model in chest and breast imaging," Linkping University, Tech. Rep. 94, 2003.

[105] MATLAB, *version 7.10.0 (R2010a)*. Natick, Massachusetts: The MathWorks Inc., 2010.

[106] L. B. Lusted, "Decision-making studies in patient management," *New England Journal of Medicine*, vol. 284, no. 8, pp. 416–424, 1971.

[107] K. Rossmann, "Modulation transfer function of radiographic systems using fluorescent screens," *JOSA*, vol. 52, no. 7, pp. 774–775, 1962.

[108] E. Samei, M. J. Flynn, and D. A. Reimann, "A method for measuring the presampled MTF of digital radiographic systems using an edge test device." *Medical physics*, vol. 25, no. 1, pp. 102–13, jan 1998.

[109] J. M. Boone and J. A. Seibert, "An analytical edge spread function model for computer fitting and subsequent calculation of the LSF and MTF," *Medical Physics*, vol. 21, no. 10, p. 1541, 1994.

[110] A. J. Kapadia, M. N. Lakshmanan, K. Krishnamurthy, P. Sahbaee, A. Chawla, S. Wolter, K. Maccabe, D. Brady, and E. Samei, "Monte-Carlo simulations of a coded-aperture x-ray scatter imaging system for molecular imaging," *Proc. of SPIE*, vol. 8668, pp. 86 680B–86 680B–6, mar 2013.

[111] M. N. Lakshmanan, J. A. Greenberg, E. Samei, and A. J. Kapadia, "Design and implementation of coded aperture coherent scatter spectral imaging of cancerous and healthy breast tissue samples," *SPIE Journal of Medical Imaging*, 2015, submitted.

[112] J. A. Greenberg, K. Krishnamurthy, M. Lakshmanan, K. MacCabe, S. Wolter, A. Kapadia, and D. Brady, "Coding and sampling for compressive x-ray diffraction tomography," vol. 8858, 2013, pp. 885 813–885 813–11.

[113] C. L. Carter, C. Allen, and D. E. Henson, "Relation of tumor size, lymph node status, and survival in 24,740 breast cancer cases." *Cancer*, vol. 63, no. 1, pp. 181–7, jan 1989.

[114] S. E. Singletary, "Surgical margins in patients with early-stage breast cancer treated with breast conservation therapy," *The American journal of surgery*, vol. 184, no. 5, pp. 383–393, 2002.

[115] N. A. Obuchowski and D. K. McCLISH, "Sample size determination for diagnostic accuracy studies involving binormal roc curve indices," *Statistics in medicine*, vol. 16, no. 13, pp. 1529–1542, 1997.

[116] T. F. Chan and L. A. Vese, "Active contours without edges." *IEEE transactions on image processing : a publication of the IEEE Signal Processing Society*, vol. 10, no. 2, pp. 266–77, jan 2001.

[117] S. Lankton and A. Tannenbaum, "Localizing region-based active contours," *Image Processing, IEEE Transactions on*, vol. 17, no. 11, pp. 2029–2039, 2008.

[118] M. S. Moran, S. J. Schnitt, A. E. Giuliano, J. R. Harris, S. a. Khan, J. Horton, S. Klimberg, M. Chavez-MacGregor, G. Freedman, N. Houssami, P. L. Johnson, and M. Morrow, "Society of Surgical Oncology-American Society for Radiation Oncology consensus guideline on margins for breast-conserving surgery with whole-breast irradiation in stages I and II invasive breast cancer." *International journal of radiation oncology, biology, physics*, vol. 88, no. 3, pp. 553–64, mar 2014.

[119] K. Hajian-Tilaki, "Receiver operating characteristic (roc) curve analysis for medical diagnostic test evaluation," *Caspian journal of internal medicine*, vol. 4, no. 2, p. 627, 2013.

[120] M. N. Lakshmanan, J. A. Greenberg, E. Samei, and A. J. Kapadia, "Experimental implementation of coded aperture coherent scatter spectral imaging of cancerous and healthy breast tissue samples," in *Proc. SPIE*, vol. 9412, 2015, pp. 94 121F–94 121F–6.

[121] R. Morris, A. Albanese, M. Lakshmanan, M. S., J. A. Greenberg, E. Samei, and A. Kapadia, "Validation of coded aperture coherent scatter spectral imaging for normal and neoplastic breast tissues via surgical pathology," 2016.

[122] A. H. Fischer, K. A. Jacobson, J. Rose, and R. Zeller, "Hematoxylin and eosin staining of tissue and cell sections," *Cold Spring Harbor Protocols*, vol. 2008, no. 5, pp. pdb–prot4986, 2008.

[123] S. Osher, M. Burger, D. Goldfarb, J. Xu, and W. Yin, "An iterative regularization method for total variation-based image restoration," *Multiscale Modeling & Simulation*, vol. 4, no. 2, pp. 460–489, 2005.

[124] G.-H. Chen, J. Tang, and S. Leng, "Prior image constrained compressed sensing (piccs): a method to accurately reconstruct dynamic ct images from highly undersampled projection data sets," *Medical physics*, vol. 35, no. 2, pp. 660–663, 2008.

[125] E. Y. Sidky and X. Pan, "Image reconstruction in circular cone-beam computed tomography by constrained, total-variation minimization," *Physics in medicine and biology*, vol. 53, no. 17, p. 4777, 2008.

Biography

Manu Nachiappan Lakshmanan
Born April 19, 1987, Temple, TX

Education
Duke University, Durham, NC, Ph.D., Biomedical Engineering, December 2015
Cornell University, Ithaca, NY, B.A., Physics, May 2009

Peer-Reviewed Publications
[1] **M.N. Lakshmanan**, S.L. Meier, R.S. Meier, R. Lakshmanan, *Psychiatry MMC* (Edgemont) 2010; 7(7):33-37. PMCID: PMC2922364.
[2] I.V. Bazarov, A.K. Kim, **M.N. Lakshmanan**, J.M. Maxson, *Phys. Rev. ST Accel. Beams*, 14(7):072001, 2011.
[3] **M.N. Lakshmanan**, A.J. Kapadia, *IEEE Trans. Med. Imag.*, 31(7):1426-1435, 2012.
[4] **MN Lakshmanan**, BP Harrawood, G Rusev, GA Agasthya, G Rusev, AJ Kapadia, *Nucl. Instrum. Meth. A*, 763:89-96, 2014.
[5] **MN Lakshmanan**, B Harrawood, G Agasthya, A Kapadia, *IEEE Trans. Med. Imag.*, 33(2): 546-555, 2014.
[6] **MN Lakshmanan**, et al.,*Nucl. Instrum. Meth. B*, 335:31-38, 2014.
[7] BP Harrawood, G Agasthya, **MN Lakshmanan**, G Raterman, AJ Kapadia, *Nucl. Instrum. Meth. A*, 764:11-17, 2014.
[8] **MN Lakshmanan**, BP Harrawood, E Samei, AJ Kapadia, *Phys. Med. Biol.*, 60(16): 6355, 2015.